In vitro detection of apoptosis using superparamagnetic iron oxide nanoparticles and molecular magnetic resonance imaging

By

Katy Rich

A Thesis Submitted to the Faculty of Physics in Partial Fulfillment of the Requirements for the Degree of

MASTER OF SCIENCE

January 13, 2010

Advised by Dr. Patrick Rapley, Ph.D. FCCPM

Department of Physics
Lakehead University
Thunder Bay, Ontario

Acknowledgements

I have many great people in my life who have been encouraging and supportive throughout my studies. First and foremost, I would like to thank my advisor Dr. Patrick Rapley who allowed me to be apart of his research over the past four years. I was able to take advantage of his knowledge and for that I am very grateful. He has always been ready and willing to give his full attention even during his busy schedule. He has been patient, kind, supportive and motivational throughout this entire experience. For these reasons, working together has been very enjoyable.

Secondly, I would like to thank Dr. Mary Lynn Tassotto for always offering helpful experimental advice and for sharing her enthusiasm for research with me. She has been a major contributor to this investigation and her expertise was a necessity. Also, I would like to thank Chris Witiw who was able to set standards for the experimental procedures and who was able to give direction for my studies by generating preliminary results.

Thank you to my committee members; Dr. Apichart Linhananta and Dr. William Sears for revision of this document and to NCRF for the funding required for this research.

Last but not least I would like to thank my family. With their love and encouragement I was able to reach my goals. They have provided me with continual support and will always do so in whichever path I choose. They are the reason I am who I am today and for this reason, I wish to dedicate my thesis to them

Table of Contents

List of Figures

List of Tables

List of Abbreviations

SPIO	Superparamagnetic iron oxide nanoparticle
PS	Phosphatidylserine
MRI	Magnetic Resonance Imaging
mMRI	Molecular magnetic resonance imaging
RF	radiofrequency
FITC	Fluorescein isothiocyanate
DNA	Deoxyribonucleic acid
MR	Magnetic resonance
TE	Echo time
TI	Inversion time
TR	Repetition time
VAC-α	Vascular anticoagulant protein alpha
FBS	Fetal Bovine Serum
CA	Contrast agent
USPIO	Ultrasmall SPIO
MION	Monocrystalline ironoxide nanoparticle
MRS	Magnetic resonance spectroscopy
OI	Optical imaging
US	Ultrasound
PET	Positron emission tomography
SPECT	Single photon emission computed tomography
Tc	Technetium
HL-60	Human Leukemia cell line
ATCC	American type culture collection
DMM	Dulbecco's modified medium
FBS	Fetal bovine serum
BL	Burkitt lymphoma cell line
ROI	Region of interest
SI	Signal intensity
FOV	Field of view
MESE	Multiple echo spin echo sequence
ICAP/ICP	Inductively coupled argon plasma spectrometer
NRC-IBC	National Research council of Canada Institute for Biodiagnostics
FDA	Food and Drug Administration
PBS	Dulbecco's phosphate buttered saline

Abstract

Superparamagnetic iron oxide (SPIO) nanoparticles have the potential to greatly expand current anatomical imaging techniques, specifically MRI. SPIO nanoparticles targeted to phosphatidylserine (PS) have the potential to detect cell death *in vitro*. In this investigation, a method for detecting apoptosis was developed using annexin V for targeting SPIO nanoparticles to PS thus enabling us to detect different levels of cell death using a clinical MRI. The results demonstrated that the presence of MACS MicroBeads (annexin V-SPIO) leads to an increase in image contrast in the regions of large numbers of apoptotic cells. The relationship between the transverse relaxation rate (R_2) and the level of apoptosis (ranging from 5-100%) was determined to be $y = 1.945 + 0.187x - 0.002x^2 + 1.161E^{-5}x^3$ ($R^2 = 0.523$) for cells tagged with annexin V-SPIO and $y = 1.570 - 0.013x + 1.918E^{-4}x^2 - 8.8680E^{-7}x^3$ ($R^2 = 0.085$) for cells untagged. Results show poor agreement with theoretical predictions but still offer potential improvement over previous efforts using SPECT imaging. The work presented here has implications for future studies of cancer treatment response and may one day help detect and quantify the levels of apoptosis in order to modify treatment according to specific patient needs.

1. Literature Review

1.1. Introduction

Cancer is a cellular phenomenon of uncontrolled growth of cells. If the growth of cells becomes uncontrolled the cells pile up and form large masses of cells called tumours. Not all tumours are seriously harmful. If the body is able to keep the tumour from spreading and the cells remain clustered together in a single mass, the tumour is said to be benign. Other tumours, called malignant, invade the body and destroy normal body tissues and organs. In advanced stages of cancer, malignant tumours may develop the ability to spread to other parts of the body and initiate new tumours, a process called metastasis. The development of cancer is clearly a multi-step process caused by many issues including spontaneous mutations during cell division or mutations caused by chemicals called carcinogens, or by physical stimuli such as ultraviolet radiation or X-rays[1]. At this point, once the cell has been exposed to oxidative stress, the cell must decide whether the damage is repairable. If damage to the genetic material has occurred, disastrous mutations may follow such as the ability to induce cancer. The complex biochemical interactions and intracellular dialogues that occur between cells in the body determine whether they divide, differentiate or die. Rather than repairing any damages that may have occurred to their DNA, some cells sacrifice themselves if repairing introduces a risk of mistakes in DNA[2].

Different cancer types behave differently. They grow at different rates and respond to different treatments. The general approaches to the treatment of cancer include surgery, chemotherapy and radiation therapy, which aim to eradicate all cancer cells from the body by physical removal or by exposure to ionizing radiation and

cytotoxic chemicals[3]. Every person will have different reactions to the different types of treatment for cancer. Therefore a technique to detect and monitor the size and location of a tumour, and image the therapeutic response of cancer cells, would be very useful in order to maximize the benefits of cancer treatment on a patient by patient basis. This thesis describes an investigation of an imaging technique with the potential to detect, characterize, stage and monitor therapeutic response which will positively impact the lives of cancer patients[37].

The introduction describes background information that is of relevance to this project. The first topic of interest explains the apoptotic pathway induced by cancer treatment modalities and its morphology including the expression of phosphatidylserine. Next, annexin V and its importance in the detection and measurement of apoptosis is discussed. Finally, how magnetic resonance imaging (MRI) in combination with a superparamagnetic nanoparticle has the ability to create a molecular imaging technique with enhanced sensitivity is overviewed.

1.2. Apoptosis Overview

In 1972, John Kerr, an Australian pathologist, recognized that following acute ligation of the portal vein in rats some cells appeared to shrink and disappear without producing inflammation[4]. This type of cell death initially named shrinkage necrosis[5] was also found in embryogenesis, effective tumour therapy, and the withdrawal of hormonal support in endocrine organs such as the adrenal gland[6]. It has been found that there are two distinct pathways of cell death characterized by their appearance; one self-regulated and controlled by the cell (programmed cell death) and the other not (necrosis)[7]. Both pathways are shown in Figure 1. James Cormack (professor of Greek) renamed this shrinkage necrosis or programmed cell death as "apoptosis" [7] which is derived from two Greek words which together translate to "from falling" to describe this type of death[5] referring to leaves falling from a tree in autumn[3]. If severe damage to a cell occurs, the cell may undergo necrosis, which involves rapid bioenergetic deterioration, inflammation and lysis (a process which is poorly regulated). Inflammation does not occur in apoptosis since the cell membrane remains intact keeping the intracellular cytoplasmic constituents from leaking out during this process[3, 7]. Although apoptosis occurs in normal cells on a regular basis, the extent of apoptosis often is enhanced in tumours by well established treatment modalities, such as irradiation, cytotoxic chemotherapy, heating and hormone ablation[6] and thus it is an important mechanism to understand when analyzing the treatment of cancer.

Apoptosis or programmed cell death can be defined as a major pathway by which the body regulates the number and type of cells as part of the body's normal embryogenesis, development and homeostasis [5]. It is associated with many neurodegenerative diseases such as Alzheimer's, Parkinson's, and Huntington's disease, motorneuronal degeneration, multiple sclerosis, and stroke [5]. As shown in Figure 1, apoptosis is a phenomenon in which cells follow a series of genetically regulated steps leading to their own destruction caused by voluntary cell suicide (in the case of developing embryos), age, or as a consequence to damage of the cell [7]. One of the earliest stages of apoptosis involves the condensation of the cytoplasm [6] and chromatin which results in shrinkage of the cell [7]. As the condensation progresses DNA also condenses and endonuclease is used to cleave the DNA into fragments between the clumps of chromatin that are referred to as nucleosomes [7]. These fragments are multiples of about 200 DNA base pairs in length. DNA fragmentation is followed by the budding of the cell as a whole to produce membrane bound apoptotic bodies [6]. Size and composition of these apoptotic bodies vary. Many contain several DNA fragments whereas others lack a nuclear component. The cytoplasmic organelles of newly formed apoptotic bodies remain well preserved [4]. Finally, these apoptotic bodies are quickly ingested or engulfed by the specialized migrating macrophages or adjacent healthy cells by a process called phagocytosis [7]. After phagocytosis, completion of digestion takes hours [4] and this fact should be kept in mind when apoptosis is being quantified histologically. The cytoplasmic organelles may continue to look healthy and indeed may be functioning even when enclosed in a phagosome in a host cell [7]. Changes also occur to the membranes of intracellular organelles during apoptosis. The plasma membrane consists of several different

phospholipids such as phosphatidylethanolamine, sphingomyelin and phosphatidylserine[5]. During apoptosis, cells loose the polarization which regularly confines phosphatidylserine (PS) to the inner leaflet of the cell membrane thus resulting in the expression of PS on the outer leaflet of the cell membrane [5]. The polarization loss is due to the inactivation of enzymes translocase and scramblase[8, 9]. The expression of PS occurs early in apoptosis [9] and is a signaling method for apoptotic cells to inform neighbouring cells that they are undergoing the process [5] (refer to Figure 2).

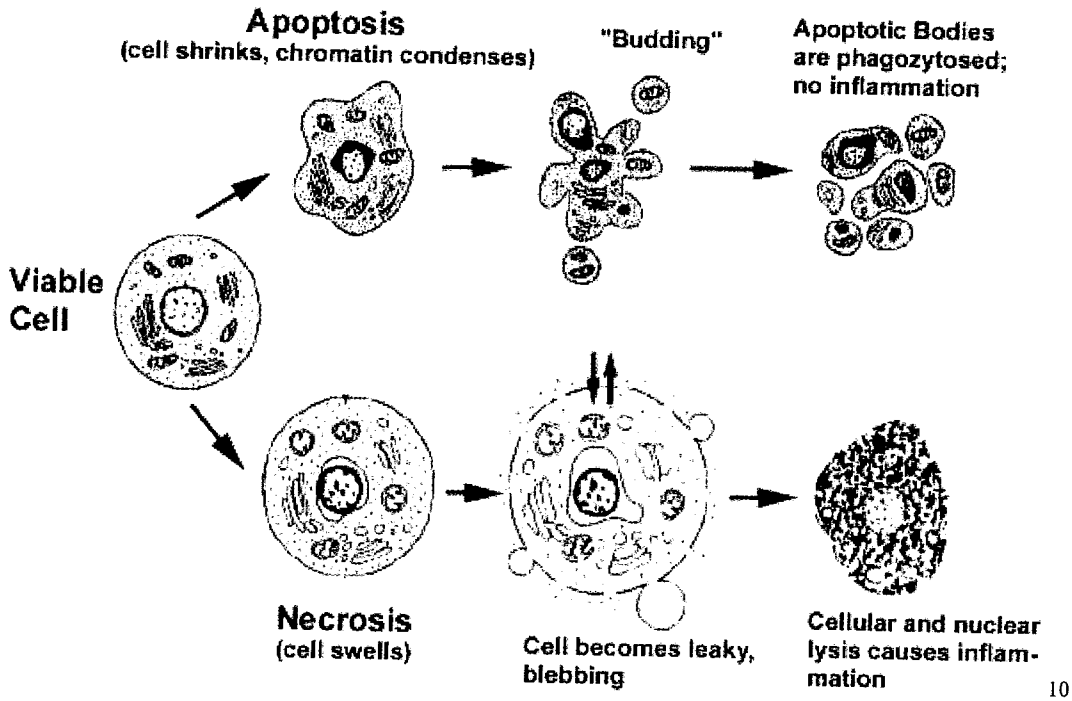

Figure 1: The apoptotic pathway (arrows above) compared to the necrotic pathway (arrows below).

1.3. Annexin V Overview

Annexin V is an endogenous human protein that belongs to the annexin family. It is approximately 32 kDa [9] and contains four domains of 70-80 amino acids arranged in a compact, water soluble structure[11]. It was first isolated from human placenta and later named a vascular anticoagulant protein alpha (VAC-α)[12]. It is one of 160 proteins that share the property of Ca^{+2} dependent binding [12] to negatively charged phospholipids like phosphatidylserine[13]. Figure 2 shows a schematic representation of the annexin V assay which demonstrates the specific binding of annexin-V to externalized PS of early apoptotic cells.

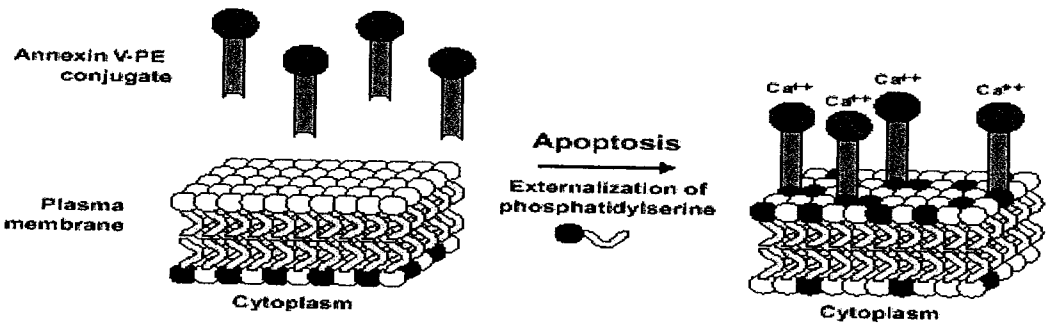

Schematic representation of the Annexin V assay.

14

Figure 2: A schematic representation of the annexin V assay BD™

Originally isolated from placenta [12], it can also be found in lower concentrations in endothelial cells, kidney, myocardium, skeletal muscle, skin, red cells, platelets and monocytes [5]. The annexin level in normal subjects is about 7ng per mL of plasma [5]. Clinical applications for annexin V are being developed in oncology, organ transplantation and cardiovascular disease [11]. Due to its high affinity for PS annexin V is therefore considered to be an excellent ligand for targeting apoptotic cells[15]. Annexin

V's efficiency as a cell label for apoptosis could be due to the fact that eight annexin V moieties can bind to one exposed PS (optimally) [8, 9]. The detection of apoptotic cells became possible *in vivo* by targeting the expression of PS with annexin V[16]. Koopman and colleagues were the first to design an apoptosis detection assay on the basis of fluorescence labeled with annexin V [12]. Annexin V has the capability to detect and quantify apoptosis [16], which could result in a significant clinical tool for diagnosis and assessment of cancer treatment.

1.4. Magnetic Resonance Imaging

Magnetic resonance imaging produces high-resolution, three dimensional maps describing morphological features of the specimen. MRI is a flexible, sensitive, non-invasive imaging technique, which utilizes magnetic fields to enable a more in depth understanding of the form and function of the human body. It is based on absorption and emission of energy.

In MRI, differential image contrast between soft tissues depends on endogenous differences in water content, relaxation times, diffusion characteristics of the tissue of interest and the introduction of exogenous contrast agents etc[17]. Relaxation is referred to as the characteristic time in which a system returns to its relaxed (equilibrium) state under certain changes in external conditions. The efficiency of the agent in enhancing the relaxation of water protons is referred to as relaxivity[1]. Most MR contrast agents rely on their ability to selectively alter the spin-lattice (T_1) and/or spin-spin (T_2) relaxation times of tissue water[18]. The most widely used MRI relaxation agents are based on gadolinium chelates that are strictly extracellular low molecular weight compounds with high T_1 relaxivity such as Magnevist[17].

1.4.1. Fundamental background theory

Magnetic resonance is a phenomenon in magnetic systems that possess magnetic moments[19]. The nucleus of an atom can be viewed as a ball of charge spinning with an angular frequency. Each element of mass contributes to the total angular momentum (J), and each element of charge contributes to the total magnetic moment (μ). Spin angular momentum (J) and magnetic moment (μ) are collinear and proportional and follow the relation:

Equation 1

$$\mu = \gamma J$$ [20]

The constant of proportionality (γ) is known as the magnetogyric or gyromagnetic ratio[20] and is defined according to its charge to mass ratio:

Equation 2

$$\gamma = \frac{q}{2m}$$ [19,]

If a linear dipole moment is present in a magnetic field (B_o) it will possess a torque that acts on μ. Application of any aligning force (torque) to a spinning object causes a circular motion known as precession[21]. Because of the presence of spin angular momentum the motion is precessional, very much like that of a gyroscope [20]. The motion of a magnetic moment vector is described as precession of μ at a constant angle α about the direction of the magnetic field B_o[22]. The frequency of precession is equal to the Larmor frequency. The Larmor frequency is described as the number of times per second

that the axis of the magnet rotates about the magnetic field direction (conventionally the z-axis)[21]. One of the most important relationships in magnetic resonance is the correlation between Larmor frequency (ω_0) and the magnetic field strength (B_0):

Equation 3

$$\omega_0 = -\gamma B_0 .$$

Reasonably, the spin should interact with an electromagnetic field rotating at the precessional frequency[20]. This relationship allows specific particles to be imaged according to their gyromagnetic ratio since it is particular and specific to each element. For example, for protons (H^1) γ = 42.6 MHz/Tesla and spins precess at f = 63.75 MHz for a 1.5 T magnetic field[23]. It is important to note that μ doesn't completely relax fully to align with the magnetic field because of thermal energy associated with the absolute temperature. Human body temperature is millions of times larger than the quantum energy difference for parallel alignment (lower energy) versus anti-parallel alignment (higher energy). There are two quantum spin states and therefore two potential alignments of spins. When the energy of a photon matches the energy difference between two spin states (hv), an absorption of energy occurs[23]. It is the resonance or exchange of energy at a specific frequency between the spins that produces the output signal[23].

Spins parallel to the magnetic field exceed anti-parallel to that field and are defined as the spin excess. If you place a human being in a magnetic field (B_o), after a period of a second or so the spins of the hydrogen nuclei (which are initially in a state of randomness) will attain some degree of order[21]. The resulting bulk magnetization will

align with B_o. The longitudinal equilibrium magnetization is then defined as the product of the total proton magnetic moment components and the spin excess:

Equation 4

$$M_0 = \frac{\rho \gamma^2 \hbar^2 B_0}{4kT} \quad 23$$

Where ρ, γ, ħ and k are all constants and T represents the temperature. This is an important relation to recognize how the magnetic field strength and the temperature can effect the total magnetization, which has a direct affect on signal strength in MRI. One can see that as the magnetic field increases so will the magnetization and it will increase even more if the temperature is decreased. For example, at 0.3 T, (at 300K) for every two million protons that are present, two more protons will align parallel with the field than anti-parallel against the field. One way to improve signal strength is to reduce the temperature of the sample but this is not very practical in biological samples. Thus, an alternative would be to use a larger magnetic field to increase signal output[20].

1.4.2. Relaxation times T_1 and T_2

The effect of an electromagnetic radio frequency (RF) pulse (applied at the Larmor frequency) is to disturb the spin system from its thermal equilibrium state. The RF coil can be placed in any direction depending on the coil design, but the RF produced by the coil must be perpendicular to the main field (z-axis). The RF produced by the coil generates a magnetic field (B_1) which forces the magnetization to rotate from the z-plane to the xy -(transverse) plane. Once the RF transmitter is turned off, three things begin to occur: the absorbed energy is now retransmitted at the resonant frequency (and can be measured as the signal), the magnetization begins to return to its original magnetization

orientation at thermal equilibrium (exponentially) and the spins begin to dephase (also exponential)[23].

The equilibrium magnetization is restored by a process known as spin-lattice relaxation. This process involves an exchange in energy between the spin system and the surrounding thermal reservoir, known as the lattice. The equilibrium is characterized by a state of polarization with magnetization M_0 directed along the longitudinal magnetic field B_0. The restoration of this equilibrium is therefore alternatively named longitudinal relaxation [24]. The rate at which the equilibrium is re-established following a perturbation of the system (ie. 90° pulse) is determined by the strength of the fluctuating pseudo-B_1 field, which greatly depends on the systems molecular dynamics[21]. The process of longitudinal or spin-lattice relaxation can be described by the following differential equation:

Equation 5

$$\frac{dM_z}{dt} = -\frac{(M_z - M_0)}{T_1}$$ [23,24]

with solution,

Equation 6

$$M_z(t) = Mz(0)\exp\left(\frac{-t}{T_1}\right) + M_0\left(1 - \exp\left(\frac{-t}{T_1}\right)\right)$$ [23]

Where $M_z(t)$ is the net magnetization in the z direction at time t, $M_z(0)$ is the initial magnetization in the z direction, M_0 is the equilibrium value of magnetization. T_1 is measured as the time required for the magnetization vector (M_z) to be restored to 63% of its original magnitude. This can be demonstrated using the plot in Figure 3A.

The process by which the net magnetization in the transverse plane of the rotating frame (rotating at the Larmor frequency) is destroyed is defined as the spin-spin relaxation. It is the process whereby nuclear spins come to thermal equilibrium among themselves [24]. For this reason, T_2 relaxation is called "transverse" or "spin-spin" relaxation. Similar mechanisms to those responsible for spin-lattice relaxation are involved such as indirect energy exchange via the lattice, but the spin-spin relaxation is dominated by interactions between spinning nuclei which are already excited. Transverse relaxation is caused by the nuclear spins spreading out due to differences in frequencies and eventually cancelling out in the xy-plane. T_2 relaxation may be exceedingly rapid in comparison with T_1 where the interaction between the nuclear spins fluctuates very slowly, as in the case of solids or rigid macromolecules. T_2 values usually fall within the range of 10 μs to 10 s [24].

The description for the transverse relaxation is written:

Equation 7

$$\frac{dM_{x,y}}{dt} = -\frac{M_{x,y}}{T_2}$$ [24]

Mx,y can be defined as the magnitude of the magnetization rotating along the x and y planes.

Since T_2 processes follow an exponential decay, the quantity T_2 is defined as the time required for the transverse magnetization vector to drop to 37% of its original magnitude after its initial excitation (see Figure 3B)[20]. Additional dephasing of the transverse magnetization is introduced by external field inhomogeneities and can sometimes be characterized by a separate decay time T_2'. The loss of transverse magnetization due to T_2' is recoverable whereas effects of T_2 are not. The effects of T_2'

can be reversed using a well known RF pulse sequence called the spin echo method. [23]

The total relaxation rate (R_2*) is defined by the sum of the external and the internal relaxation rates as follows:

Equation 8

$$R_2^* = R_2 + R_2',$$ [23]

And in terms of overall relaxation time $R_2^* = 1/T_2^*$:

Equation 9

$$\frac{1}{T2^*} = \frac{1}{T2} + \frac{1}{T2'}$$ [23]

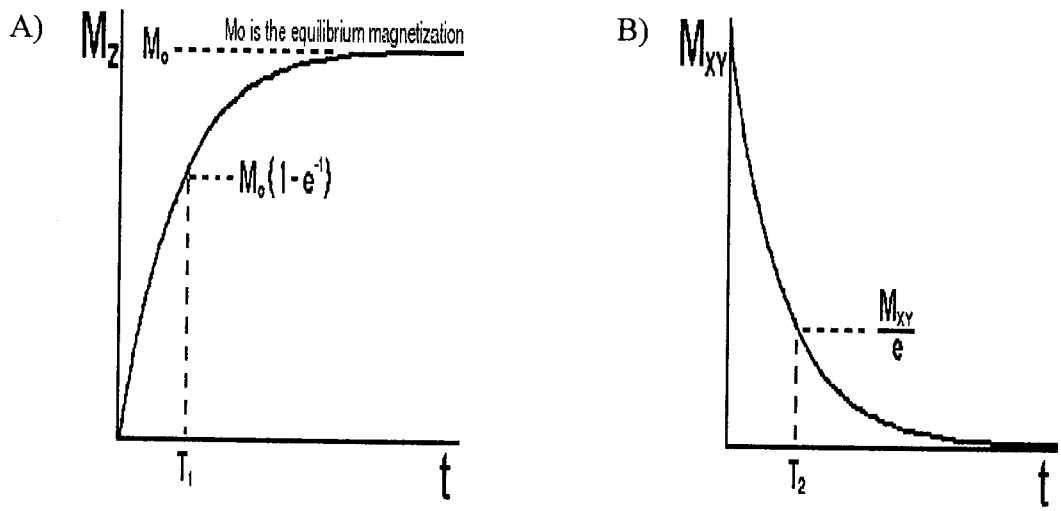

Figure 3: **A)** The spin lattice relaxation: the process by which the spin population returns to its equilibrium Boltzmann distribution following the absorption of r.f. energy. **B)** The spin-spin relaxation: the process in which the net magnetization in the x'y'-plane of the rotating frame is destroyed.

1.4.3. Molecular Magnetic Resonance Imaging

1.4.3.1. Contrast Agents in MRI

Molecular imaging can be defined as a new imaging technique designed to advance our understanding of biology and medicine using non-invasive *in vivo* imaging to investigate cellular and molecular events. Molecular imaging has the ability to expand the range of capabilities of conventional anatomical imaging methods by combining non-invasiveness and high spatial resolution with specific localization to molecular targets. The use of biomarkers provides a means of probing specific molecular targets or pathways. The specificity of regular MRI imaging can be increased by exogenous contrast agents (CA) bound to specific biomarkers, which have been successfully used for imaging otherwise undetectable molecular targets. The targeted contrast agent should recognize targeted cells with high affinity and specificity with the use of these biomarkers. To be successful, the imaging contrast agents must also efficiently gain access to these targets, show minimal non-specific uptake and retention in the body and have sufficiently long half-lives to be detectable and functional at trace concentrations[25]. In the case or molecular MRI (mMRI) the agent should also be characterized by high relaxivity (the ability to increase proton relaxation rate). To date, gadolinium (which generates a T_1 positive signal enhancement in MR images) and SPIO nanoparticles (which generate strong T_2 negative contrast (pixel darkening) in MR images) are the most commonly used materials as MRI contrast agents [31].

1.4.3.2. Molecular Targeting

Molecular MRI presents a unique non-invasive clinical opportunity to allow sensitive and specific monitoring of key molecular targets [25]. Using a combination of

ligands bound to contrast agents, specific molecular targets can be detected and monitored. For example, due to the exquisite spatial resolution of MRI with magnetic nanoparticles targeted to macrophages in lymph nodes, Harisinghani *et al* was able to detect millimetre sized metastases in non enlarged lymph nodes which is beyond the threshold of other molecular imaging techniques[26]. Depending on the choice of ligand and the contrast agent that is bound, many physiological aspects that were otherwise undetectable have been made detectable. Since SPIO nanoparticles are available pre conjugated to multiple ligands, this contrast agent could be useful in detecting multiple molecular targets.

The use of mMRI will give clinicians the ability to not only locate a tumor within the body but also visualize physiological processes of specific molecules that influence tumor behaviour and/or response to therapy [25].

1.5. Superparamagnetic iron oxide (SPIO) nanoparticles

SPIO nanoparticles typically consist of two components, an iron oxide core and a hydrophilic coating[27]. The coating is used to prevent uncontrollable aggregation and sedimentation of the particles in aqueous solutions, aids in biological tolerance and prevents toxic side effects[28]. For example dextran is used as an antithrombotic (anti platelet) and to reduce blood viscosity in clinical applications[29]. They are generally classified according to their size, typically particles >40nm in diameter are labeled SPIO nanoparticles and <40nm are labeled USPIO (ultrasmall SPIO) nanoparticles. These categories can be further divided into subgroups such as MION (monocrystalline iron oxide nanoparticles) which are approximately 10 – 30nm in diameter and Oral SPIO which are much larger having a diameter of 300nm – 3.5μm[27].

1.5.1. SPIO and the MRI

Superparamagnetism occurs when the size of a ferromagnetic material is small enough that the ambient thermal energy is sufficient to induce free rotation of the entire crystallite[29]. They can be regarded as thermodynamically independent, single domain particles[30]. SPIO nanoparticles (see Figure 4) possess large magnetic moments while in the presence of magnetic field but retain no net magnetization when the field is removed. Superparamagnetic refers to the characteristic strong paramagnetic nature of the particle, which is much stronger then strictly paramagnetic due to its single crystal nature allowing the alignment of the entire crystal with the applied field[27]. The relaxivity and biological properties of superparamagnetic nanoparticles depend strongly on their magnetic characteristics, influenced by the chemical composition, the crystal and agglomerate size and the type of coating [31]. The strong local magnetic fields introduced by these particles significantly affect the spin relaxation processes of the protons in the medium. As a result of the translational diffusion in the neighbourhood of these microspherical inclusions, solvent or water protons experience fluctuations in the local magnetic field. The component of the fluctuation at the proton resonant frequency contributes to both the spin-lattice relaxation and the spin-spin relaxation whereas the latter is also affected by low frequency components [18]. Superparamagnetic contrast agents have the advantage of producing an enhanced proton relaxation in MRI better than those produced by paramagnetic ions and thus lower doses are required to enhance microscopic effects in the human body[31]. Due to the resulting magnetic fields created by the particles in a constant magnetic field the spin relaxation process of nearby protons shortens.

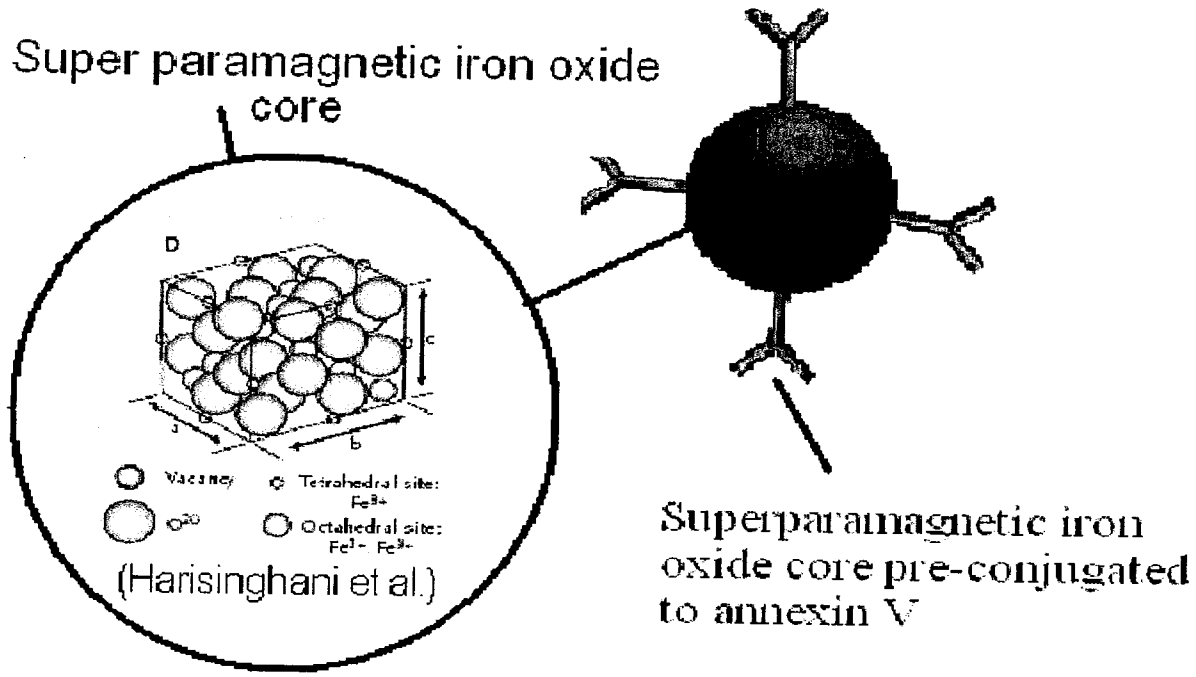

Figure 4: Superparamagnetic iron oxide nanoparticles. The iron oxide core is conjuagated to annexin V allowing to selectively target phosphatidylserine in apoptotic cells.

1.5.2. SPIO targeting

Several highly specific SPIO complexes have been characterized for their MRI relaxivity[32, 18]. Due to their iron content, basic SPIO nanoparticles are liver-targeting agents naturally taken up by the reticuloendothelial system, including Kupffer cells[33, 34]. They are used clinically to improve the detectability of focal liver lesions mainly by increasing tumor to liver contrast, and occasionally to differentiate among liver tumors such as focal nodular hyperplasias, hepatic adenomas and well-differentiated hepatocellular carcinomas [33]. In molecular imaging rather than having a natural high

affinity for a particular organ which may limit the location of the imaging, SPIO nanoparticles can be bound to ligands specific to physiological states of interest such as apoptosis. Various types of targeting ligands can be used for apoptosis detection such as proteins, peptides, optamers and small molecules that actively target specific molecular recognition of apoptosis. SPIO nanoparticles have the potential to improve and enhance the capabilities of conventional MRI modalities. Some examples of existing SPIO nanoparticles are can be found in Table 1.

Table 1: A list of iron oxide nanoparticles that are commercially available and their properties[30,34,28]

Agent	Class	Compound	Trade names	R2 (1/s)	FDA Approval	Particle size
AMI-121	Oral SPIO	Ferrumoxil	Lumirem, GastroMARK		Approved	>300 nm
OMP	Oral SPIO	Ferristene	Abdoscan		Approved	3.5 μm
AMI-25	SPIO	Ferumoxide	Feridex, Endorem	160 (0.47T)	Approved	80-150 nm
AMI-227	USPIO	Ferumoxtran	Sinerem, Combidex	80 (0.47T 37°)	Phase III	20-40 nm
NC100150	USPIO	Ferucarbotran	Clariscan		Discontinued	20 nm
SHU555A	SPIO	Ferucarbotran	Resovist, Cliavist	82.0 (1.5T 37°)	Phase III	62 nm
SHU555c	USPIO	Ferucarbotran	Supravist, Resovist S	60 (0.4T 40°)		>20nm
CODE 7228	USPIO		(Advanced magnetics)		Phase II	18-20 nm

1.6. Techniques for the detection of apoptosis

Cell death by apoptosis is considered a major pathway in the response of tumour cells to radiation and chemotherapy[35, 36]. Assays currently used to measure apoptosis include detection of morphologic changes by light microscopy, electron microscopy, or flow cytometry using nuclear staining with giemsa or fluorescent dyes [13]. The annexin V FITC assay has been described as the hallmark for the separation of necrotic cells from those undergoing apoptosis[40].

Several different non-invasive, quantitative, functional imaging techniques[37] have shown promise in imaging apoptosis including magnetic resonance spectroscopy (MRS),

magnetic resonance imaging (MRI), positron emission tomography (PET), single photon emission computed tomography (SPECT), optical imaging (OI) and ultrasound (US). Apoptosis has been detected through its enzyme expression, DNA fragmentation markers, membrane alterations, proteases, apoptotic proteins, plasma membrane leakage or metabolic activity[8]. Success of each technique derives from the ability to target these markers. In many organs only a small fraction of cells undergo apoptosis at any given moment, and thus CA-ligand complexes with an optimized conjugation, labelling chemistry and high sensitivity may be needed for its detection [38].

Nuclear imaging has been successful for the in vivo detection of apoptosis with the aid of 99mTc-radiolabeled annexin V molecules. Initially, 99mTc-labeled Annexin V was used by Tait in 1994 to detect thrombi in the atria of rabbits with atrial fibrillation[11]. This initial results in experimental animals suggested the 99mTc-rh-annexin V could be clinically useful to detect apoptosis in vivo [5]. Since the first detection of apoptosis *in vivo*[16], several 99mTc-Annexin-V-based radioligands have been developed with the potential to becoming clinically useful [8]. The limiting factors in the use of 99mTc-annexin V are rapid serum half-life (6h) [8], lack of specificity for apoptosis vs. necrosis and the somewhat low resolutions of 1-3mm [9]. MRI offers the complex differentiation between materials because of its sensitivity to proton densities, relaxation times, temperature and proton motion which is more versatile than other imaging techniques restricted to only one type of contrast[20]. The detection threshold for SPIO labelled cells depends on field strength, pulse sequence used, acquisition parameters etc. and under certain conditions, MRI cell tracking with SPIO nanoparticles can actually be more sensitive than nuclear techniques [39]. Foster-Gareau et. al. showed that single cells

labelled with SPIO nanoparticles could be imaged with a 1.5 T clinical scanner[39]. In contrast the sensitivity of nuclear techniques was limited to a few hundred cells[39].

SPIO nanoparticles demonstrate dose-dependent signal intensity reduction in T_2 weighted images and have extremely high spatial resolution. Cross-linking of SPIO nanoparticles with annexin V provides a true non-invasiveness MRI technique that may have a wide range of clinical utility in both the diagnosis and monitoring therapy of a wide range of human disorders [5].

1.7. Conclusions

There will always be a desire for new, high resolution, sensitive, non-invasive techniques aimed to improve the overall detection and treatment of cancer therapy. Molecules such as 99mTc radiolabeled annexin V have been used along with nuclear imaging *in vivo* as a non-invasive means to detect and serially image tissues and organs under going programmed cell death [20]. However, with the use of an isotope there will always be an issue with potential risk of inducing cancer, spatial resolution limitations and the length of the half-life limiting the detection. Magnetic resonance imaging does not suffer from these limitations and can be used to make high-resolution images of anatomy and function of human parts. Therefore, mMRI with the use of SPIO nanoparticles could potentially have a major impact on cancer detection, individualized treatment and drug development as well as understanding how cancer arises [25].

2. Project Summary

Molecular imaging is emerging as a potential tool for monitoring treatment response in the management of cancer patients. Recent cell biology as well as oncology research has focused on apoptosis or programmed cell death as a means of measuring these induced effects and detecting response. With an appropriate ligand and contrast agent, molecular magnetic resonance imaging (mMRI) offers the potential of a noninvasive probe for apoptosis. A hallmark of early stage apoptosis is the externalization of phosphatidylserine (PS). The human protein annexin V with its high binding affinity for PS has been used ubiquitously in the biochemistry apoptosis FITC assay[40]. As previously demonstrated in cardiomyocyte cells[41], annexin V + SPIO nanoparticles can provide sufficient MRI T_2 and T_2* contrast enhancement for in-vivo detection of apoptosis. The aim of the present study was to demonstrate the feasibility of imaging the therapeutic response of cancer cells by establishing a quantitative relationship between T_2 enhancement and apoptotic extent. Specifically, heat shock induced apoptosis in human leukemia HL60 cells in-vitro was probed by tagging with Annexin V+SPIO and subsequent analysis of the transverse relaxation (T_2) measured with a multi echo spin echo MRI acquisition. This characteristic of apoptosis was chosen based on their ability to be probed with annexin V which is readily available to the laboratory pre-conjugated to several contrast agents. Thus, if pre-conjugated to an MRI contrast agent, annexin V has the ability to bind to apoptotic cells *in vivo*, and as a result the amount of cell death can be quantified. This is only one of the many capabilities of annexin V. There exists many possible physiological states that can be detected using ligand-SPIO complexes.

2.1. Hypothesis:

Molecular MRI with SPIO nanoparticles can be used to quantify the degree of apoptotic damage in treated HL-60 cells. This method could be feasible for assessment of response to cancer treatment.

2.2. Objectives:

There are many smaller objectives that were addressed in order to demonstrate the feasibility of imaging the therapeutic response of cancer cells by establishing a quantitative relationship between T_2 enhancement and apoptotic extent. Specifically,

- ✓ Analyze the effect of SPIO nanoparticle concentration on MRI output signal intensity (SI) and the relaxation rates (R_1 & R_2) produced, also determining what magnetic field strength is required for best contrast.
- ✓ Determine a treatment method of inducing 100 percent apoptosis.
- ✓ Optimize the concentration of cells that will produce the greatest differentiation between apoptotic (treated) and healthy (untreated) cells in sensitivity.
- ✓ Determine the feasibility of quantifying apoptotic percentage of treated HL-60 cells using the relaxation rate effects produced by SPIO nanoparticles.
- ✓ Find the corresponding relationship between relaxation rate enhancement and apoptotic percentage and determine if this tool is reproducible and potentially useful in clinical studies.

3. Materials and Methods

3.1. Introduction

In order to detect early stage apoptosis, a number of methods were used. This thesis has been broken down into several specific experiments in order to collectively complete our objectives and prove the hypothesis. Some general techniques have been used throughout each section and thus they will be described first. The methods for each step are explained in further detail in each specific experiment subgroup. The specific experiments that were investigated are:

- *SPIO concentration T_1 & T_2 calibration (section 4.1),*
- *Feasibility percent apoptosis gradient (section 4.2),*
- *The effect of cell concentration on sensitivity of apoptotic percent measurement (section 4.3),*
- *Detection of 100 percent apoptosis with PS bound SPIO nanoparticles (section 4.4),*
- *Percent apoptosis gradient using heat shock (section 4.5),*
- *Reproducibility study: percent apoptosis gradient (section 4.6),*

The materials and methods, results and discussions of the specific experiments will be described in section 4.

3.2. General Techniques

3.2.1. Cell Culture Conditions

This study used the human leukemia (HL-60) cell line, which along with cell handling training and guidance, was kindly provided by Dr. M.L. Tassotto. The cell line was originally obtained from the American Type Culture Collection (ATCC). This cell

line was maintained in a humidified atmosphere at 37°C and 5% CO_2. They were propagated in Dulbecco's Modified Medium (DMM, Sigma Aldrich 1763) supplemented with 10% Fetal Bovine Serum (FBS), sodium bicarbonate (3.024 g, $NaHCO_3$) and antibiotic/antimycotic (100 units/ml penicillin G Sodium, 100 μg/ml streptomycin sulfate, 0.25 μg/ml amphotericin B). Cell cultures were maintained in 75 cm^2 tissue culture flasks. Medium was renewed every two or three days and cells were subcultured to maintain a concentration of no greater than 1.2 million cells per mL.

3.2.2. Heat shock procedure

The cells were initially counted with a coulter counter in order to calculate the concentration and total number of cells present in a sample. From this information, the cells can be split into known populations depending on the amount of cells required to be treated and left untreated. Depending on the specific experiment, the predetermined number of cells (still suspended in their medium) was then placed in a 65°C water bath for 15 minutes in order to induce apoptosis. Post heat shock, the cells were allowed to recover for one hour in an incubator set at 35°C.

3.2.3. *Cell Staining*

After induction of apoptosis, the cells are stained with either MACS Annexin V-FITC kit (Miltenyi Biotech) to be analyzed with flow cytometry or stained with MACS Annexin V-MicroBeads kit (Miltenyi Biotech) to be analyzed by the MRI (see Figure 5).

The general protocol for MACS Annexin V-FITC kit involves washing 10^6 cells in 1 mL 1 x binding buffer (provided by Miltenyi) and centrifuging at 300 xg for 10 minutes. After removing the supernatant completely, the pellet is resuspended in 100 μL of 1 x binding buffer per 10^6 cells. Finally, add 10 μL of annexin V-FITC per 10^6 cells,

mix well and incubate for 15 minutes in the dark at room temperature. Wash cells by adding 1 mL of binding buffer per 10^6 cells and centrifuge at 300 xg for 10 minutes. The supernatant is removed once again and the cells are washed repeating the last step.

The protocol for enrichment of annexin V-SPIO includes taking a population of the cells and centrifuging at 300 xg for 10 minutes. Then remove the supernatant completely and resuspend the cell pellet in 80 µL of 1 x binding buffer per 10^7 cells. Next, add 20 µL of MACS Annexin V MicroBeads per 10^7 total cells, mix well and incubate for 15 minutes at 6-12 °C. Finally, the cells were washed by adding 10-20x the labeling volume of 1 x binding buffer (1-2 mL per 10^7 cells), centrifuge at 300 xg for 10 minutes, remove the supernatant completely and then repeat the wash 3 times to remove excess unbound annexin V-SPIO. This sample of cells was prepared and then analyzed by the MRI.

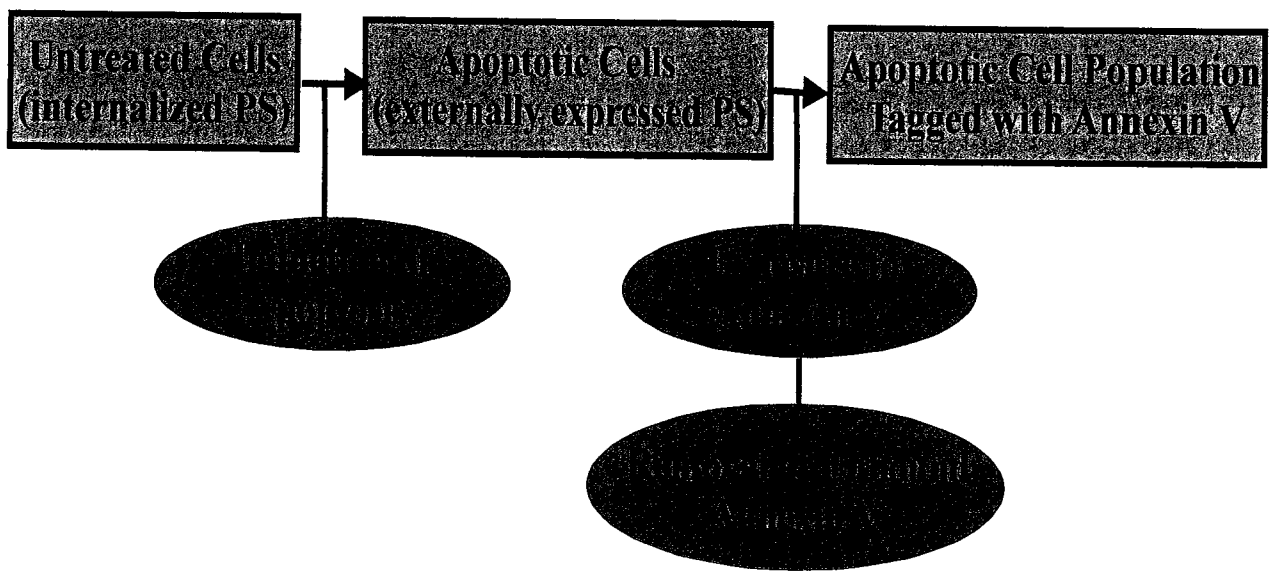

Figure 5: Flow chart indicating the method of staining apoptotic cells with annexin V.

3.2.4. Flow Cytometry

Flow cytometry is a technique for counting and examining microscopic particles. It allows simultaneous multiparametric analysis of the physical and/or chemical characteristics of single cells flowing through an optical and/or electronic detection apparatus. This device uses the principles of light scattering, light excitation and emission of fluorochrome molecules to generate specific multiparameter data from particles and cells in the size of 0.5μm to 40μm diameter. Cells are hydro dynamically focused in a sheath of PBS before intercepting an optimally focused light source. The detection of apoptosis on a per-cell basis by flow cytometry has previously been recognized by Koopman in 1994 when he quantified Burkitt lymphoma (BL) cells with fluorescein isothiocyanate (FITC)-labeled annexin V [13]. Since then, annexin V has been used ubiquitously for the benchtop biochemical assay for apoptosis. In this work, the cells were analyzed by flow cytometry using a FACS Calibur flow cytometer (Becton Dickinson) following procedure defined by Miltenyi Biotech (detailed in section 3.2.3). The level of apoptosis was determined based on the staining of the cells to annexin V-FITC and comparison of the results to previously determined controls shown in Figure 6. The results are analyzed using single colour histogram analysis which plots fluorescence intensity (FL1) versus cell count. Markers are used to quantify the population of cells that exist in each portion of the histogram. Cells that are detected in the first marker (M1) are said to be annexin V negative (since they have less fluorescence detected in that population), and cells that are detected in the second marker (M2) are said to be annexin V positive (since the fluorescence is becoming more visual thus detecting many apoptotic cells) and therefore the level of apoptosis can be calculated with this result (see Figure 6).

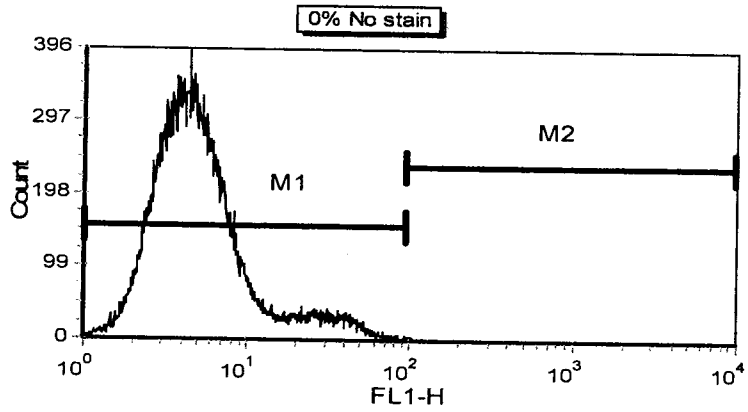

Parameter	Marker	# of Events	% of all cells
FL1-H	M1	624	1.25
FL1-H	M2	49374	98.75

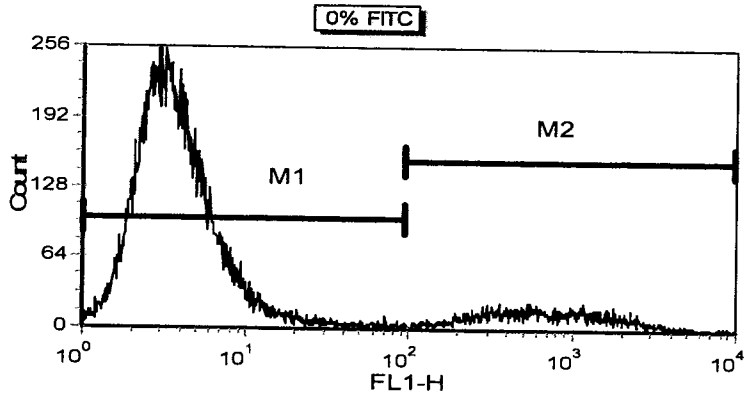

Parameter	Marker	# of Events	% of all cells
FL1-H	M1	31784	87.02
FL1-H	M2	4740	12.98

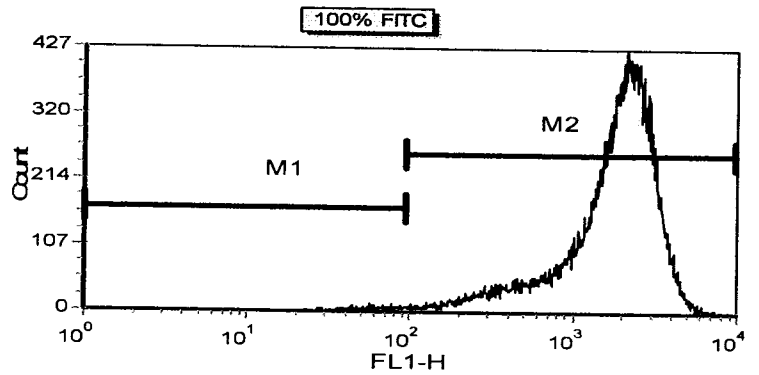

Parameter	Marker	# of Events	% of all cells
FL1-H	M1	49907	99.81
FL1-H	M2	93	0.19

Figure 6: Controls for analysis by flow cytometry. Apoptosis is indicated by the population of annexin V positive cells in the M2 marker on the histograms with approximately 50000 cells counted. A) 0% apoptosis with no annexin staining measures 0.19%, B) 0% apoptosis with annexin-V-FITC staining measures 12.98%, C) 100% apoptosis with annexin-V-FITC staining measures 98.75%.

3.2.5. MRI Gel Sample Preparation

A 1% carrageenan gel was prepared by mixing 0.1 g of carrageenan (Sigma Aldrich) with 10mL of PBS (Dulbecco's phosphate buttered saline) heated to approximately 90°C. In order to ensure a uniform distribution the gel was mixed thoroughly using a vortex stirrer prior to polymerization. In order to maintain the 90°C temperature required to keep the gel from solidifying, the gel was divided into smaller 1.5 mL microfuge tubes and placed in a block heater. Cell populations were then resuspended in the gel, mixed with a vortex again, and placed in a 384-well microplate in volumes of 100μL. Precise pipetting was performed to ensure no air bubbles from forming in the wells and attempts were made to prevent the gel from clumping in the tips of the pipettes. A map of the layout of the location of the specific cell populations was created in order to cross reference with the MR images during the MR procedures. Carrageenan is a previously developed MRI gel material phantom with T_1 and T_2 relaxation times similar to those of the human body at 1.5T and is also useful as a T_2 modifier[42].

3.2.6. MRI

Since relaxation times (along with many other properties) effect the intensity of the MRI image produced, an investigation of T_1 and T_2 with several imaging sequences must occur. Samples that were placed in 384-well microplates (as described in section 3.2.5), were scanned in the clinical MRI (1.5 Tesla Siemens Avanto Clinical MRI scanner) located at the Thunder Bay Regional Health Sciences Centre. Although several coils were utilized in early investigations (ie. head and knee), the best overall signal was produced with the use of a wrist coil. Figure 7 shows how the 384-well microplate (filled

with gel samples) was placed in the wrist coil prior to being placed in the MRI to be imaged.

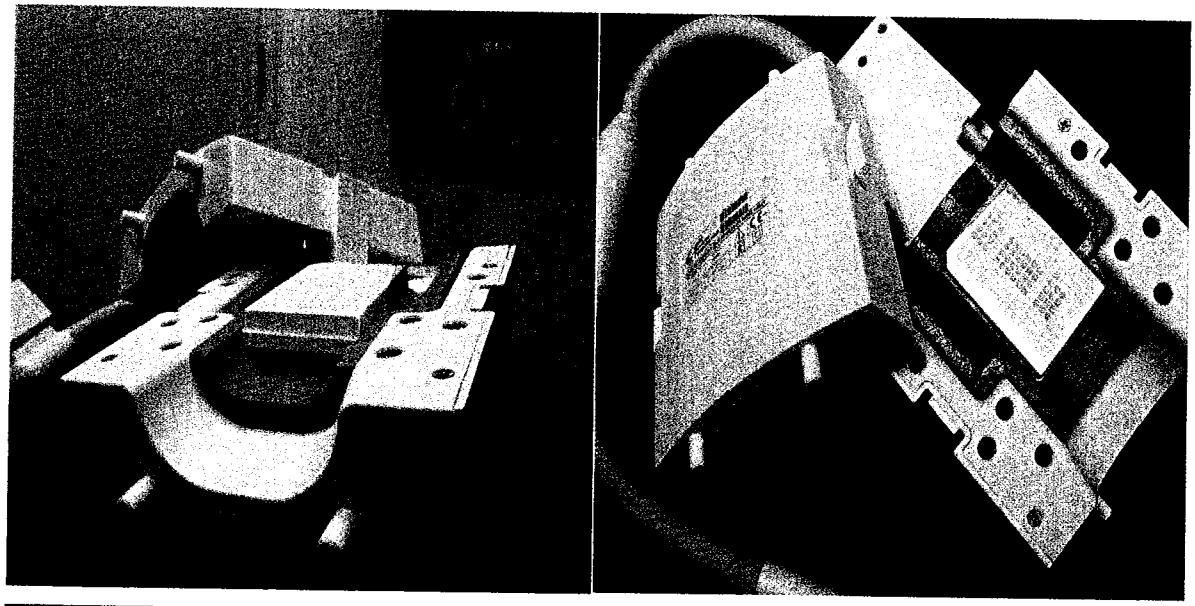

Figure 7: Gel samples placed in the wrist coil prior to MR imaging.

Siemens proprietary image manipulation software was used to process pixel and region of interest (ROI) data to extract quantitative T_1 or T_2 values. Using Siemens interactive ROI tool, the ROIs were selected to cover approximately 80 % of the area of the well sample. Standard deviations were recorded and accurately propagated to produce error in the relaxation times. The sequences used to measure T_1 and T_2 are described in the next section. The resolution, field of view and slice thickness were optimized for each specific experiment in the study and will be described in the relevant specific experiment section.

3.2.6.1.Measurement of T_1 and T_2

T_1 relaxation time can be measured by various techniques. The most common pulse sequence for measuring T_1 is inversion recovery (see Figure 8) since it is both simple and reliable. It consists of a 180° pulse to invert the magnetization followed by a variable time delay TI during which the z component of the bulk magnetization "recovers" from $-M_0z$ to its equilibrium value of $+M_0z$. This recovery which is dominated by the spin lattice relaxation process is characterized by the T_1 time constant. If TI is varied over a suitable range in repeat image acquisitions, the spin-lattice relaxation time for a given ROI can be found by performing an exponential fit on the series of ROI data. T_1 can then be calculated using the following relationship:

Equation 10

$$S(TI) \propto M_z(TI) = M_0\left(1 - 2\exp\left(\frac{-TI}{T_1}\right)\right) \quad (20)$$

$M_z(TI)$ is the magnetization in the z direction at a specific time delay TI, M_0 is the equilibrium magnetization and S(TI) is the signal strength (pixel by pixel of ROI). At room temperature T_1 is usually in the range of 0.2-1.2 seconds for protons in abdominal tissue[20].

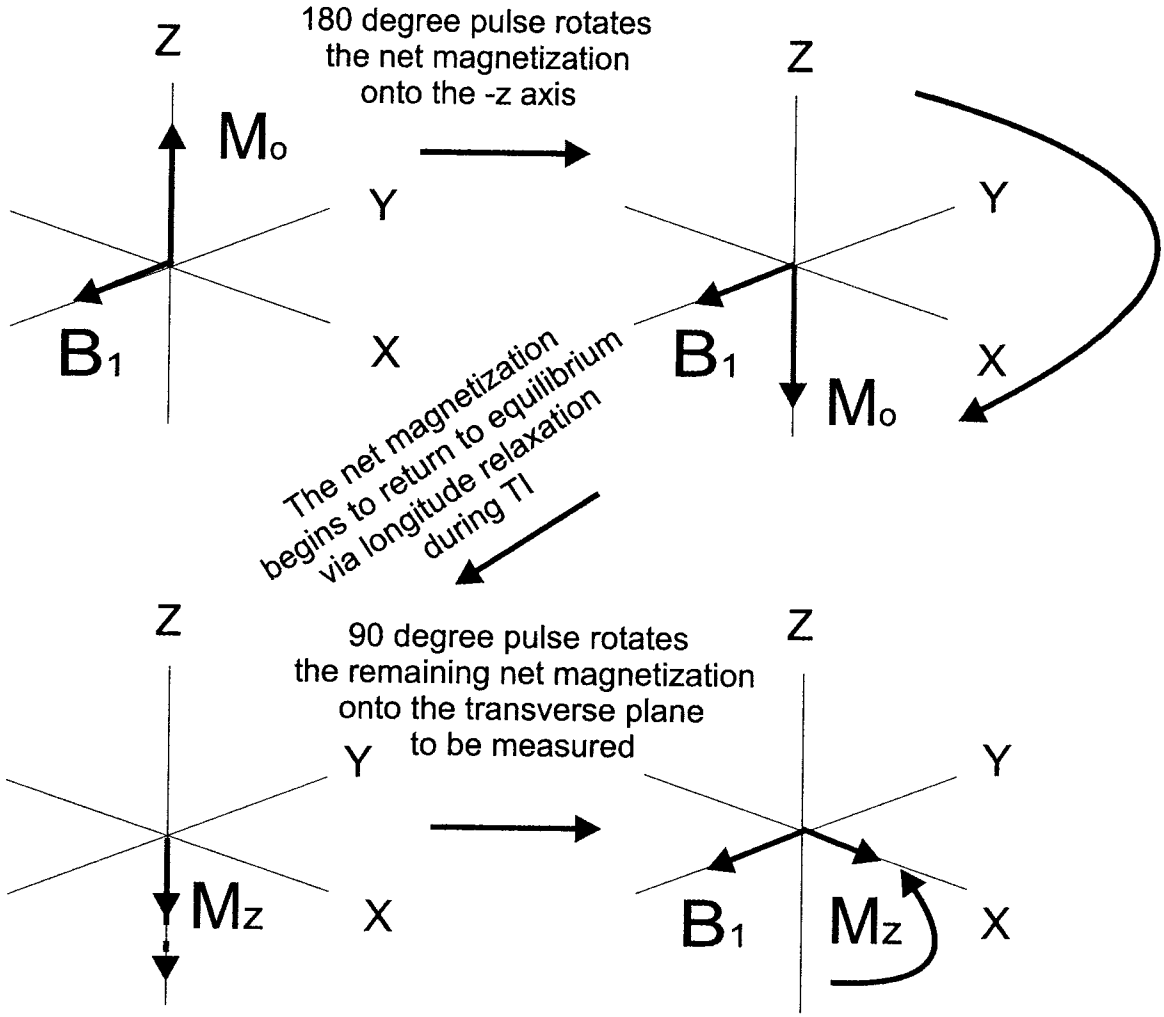

Figure 8: Inversion recovery sequence including a 180° pulse, a time delay TI and a 90° pulse.

When choosing an MRI sequence to measure T_2 relaxation time, a decision must be made whether to account for additional dephasing introduced by external field inhomogeneities. The decay due to external magnetic field inhomogeneities is a coherent process, which can be eliminated using a spin-echo sequence and can be shown in Figure 9. The simplest example of this type of experiment is one in which only two RF pulses are required. The spin echo sequence uses a 90° pulse to excite the magnetization onto

the transverse plane (x or y axis depending on the location of the applied field B_1) and at this time the isocromats begin to dephase. This process is allowed to continue for a time (TE/2) at which this point a 180° pulse is applied to refocus the coherent portion of the spins to generate signal echoes called spin echoes. The time between the 90° pulse and the refocusing of the spins is called the echo time (TE). In a spin echo acquisition, the image pixel intensity is directly proportional to the amplitude of the signal spin echo. The relationship between the signal intensity and TE is shown to depend on the samples T_2 as in equation 9. Through the addition of further 180° pulses (at intervals of TE) produces a series of echoes of alternating sign and allows T_2 to be determined in a single experiment.

T_2 can be calculated using the solution to the about relationship:

Equation 11

$$S_{x.y}(TE) \propto M_{x,y}(t) = M_{x,y}(0)\exp\left(-\frac{TE}{T_2}\right) \quad (5, 24)$$

$M_{x,y}(t)$ is the magnetization in the transverse axis (x-y plane), $M_{x,y}(0)$ is the initial magnetization on the x-y plane following the 90° pulse and $S_{xy}(TE)$ is the signal strength at time TE. A 16-echo spin-echo imaging sequence (see Figure 10) was used with echo times (TE) varying depending on the specific experiment.

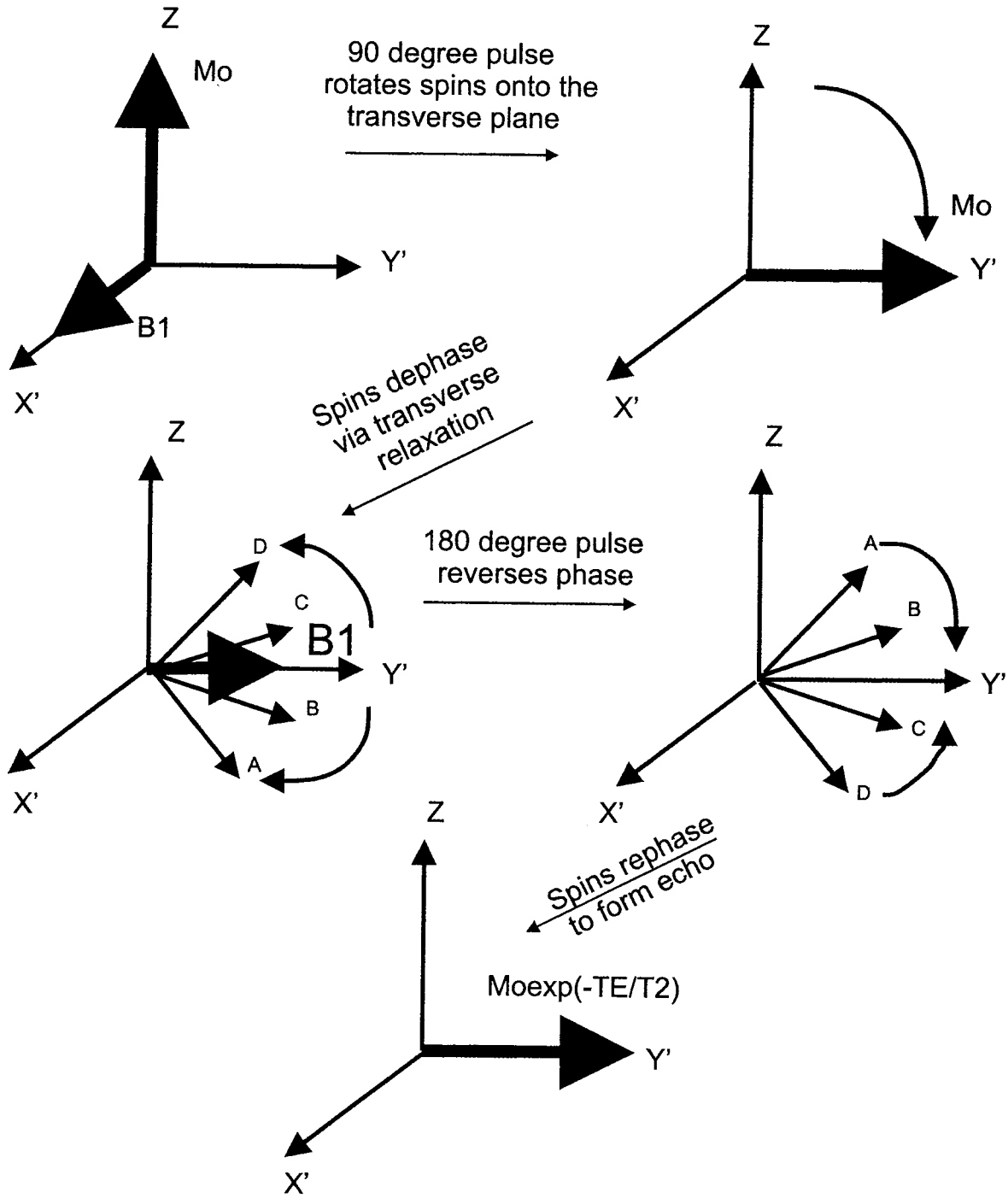

Figure 9: Spin echo imaging sequence displaying spins and pulses created in order to measure the spin-spin relaxation time (T_2). The echo time (TE) is defined as the time between the initial 90° pulse and the formation of the echo. The intrinsic T_2 decay will cause a reduction in echo amplitude.

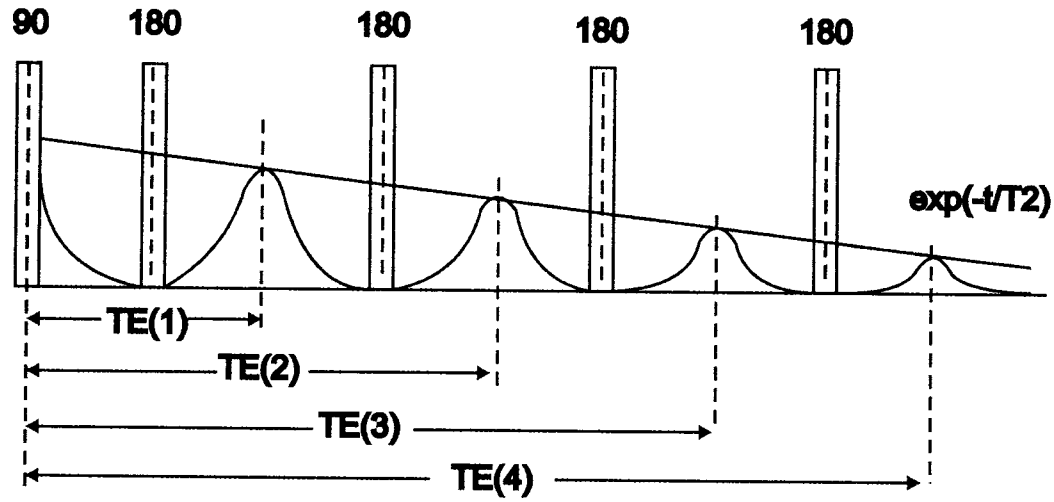

Figure 10: Multiple spin echo sequence in which repeated 180° pulses successively recall signal to give echoes at times nTE. T_2 decay envelope shown to have curve fit of $\exp(-t/T_2)$[20].

3.2.6.2.Manual Determination of T_1 & T_2

The pixel and region of interest data was processed with image manipulation software to extract quantitative T_1 & T_2 enhancement relative to background image. In an attempt to avoid interference issues, quantitative analysis was extracted from the image using regions of interest occupying approximately 80% of the area. From these regions of interest, mean pixel intensity and standard deviations of the MR intensity were extracted and plotted versus echo time (TE) (for T_2) and inversion time (TI) (for T_1). These variables form exponential decay plots as the signal decreases. Exponential curve fit analysis was performed and from equation 9 & 10 quantitative T_2 and T_1 values are calculated. The signal intensities (extracted from ROIs) are plotted versus echo times to determine the relaxation times of each sample. Since the signal intensity and echo time relationship is defined as exponential decay (see equation 9) rather than doing an exponential curve analysis a quick way to avoid this would be to plot the logarithm of the

signal intensities versus the echo times (or inversion time for T_1) as seen in Figure 11. This relationship will generate a linear trend with the slope determining the final relaxation time for that sample. Using a sample that has 8.57% apoptosis the equation of best fit between log(signal intensity) and echo time was determined to be $y = 2.748 - 0.00723x$. With this results we can then calculate the T_2 value using the slope since $m = -1/T_2$, therefore $T_2 = 1/0.00723 = 138.3$ ms. After calculating T_1 and T_2 for each sample, a relationship was then found between the relaxation times and the percentage of apoptosis determined from the flow cytometry results.

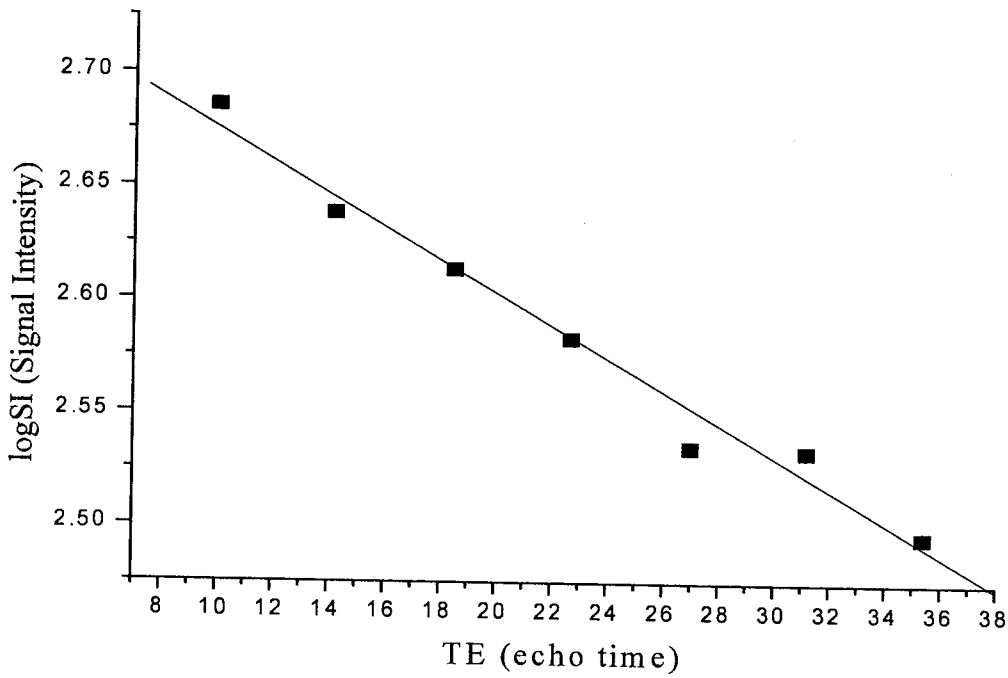

Figure 11: Manual exponential fitting for determination of T_2. Log of Signal intensity (SI) versus echo time (TE) has been defined by the relationship: $\log SI = \log[\rho \exp(-TE/T_2)]$ (equation 10). TE is defined in ms in this example. Note: to determine T_1, SI is plotted vs TI rather than TE.

3.2.6.3. Determination of T_2 using Leonardo Software

The Leonardo (Siemens post processing) image manipulation software is capable of performing exponential T_2 analysis on a series of images acquired in the multiple echo spin echo sequence. This has the advantage of reducing time of analysis. With this software, a T_2 examination is performed, and the manual exponentially T_2 fitting was eliminated. Siemens post processing was then used once again to process pixel and region of interest data. The regions of interest (ROIs) were used to extract T_2 values and R_2 values were obtained by taking the inverse of an average of 5 ROIs (T_2 values) taken from 5 separate wells. Standard deviations were recorded and accurately propagated to produce error in the relaxation times. The Siemens post processing software was used throughout the specific experiments and verified using the manual method.

4. Specific Experiments

An attempt has been made to measure the extent of apoptotic damage in HL-60 cells using SPIO nanoparticles and mMRI. A commercially available Annexin V ligand + SPIO contrast agent conjugate and 1.5T clinical MRI scanner was applied to establish the relationship between the level of apoptotic damage and MRI signal enhancement.

Included are results of several investigations regarding relaxation effects:

- ✓ as a function of SPIO concentration (section 4.1)
- ✓ as a function of cell concentration, (section 4.4) and
- ✓ as a function of percent apoptosis (section 4.2, 4.5 & 4.6).

These investigations will provide the evidence necessary to determine whether the technique of detecting apoptosis in HL-60 cells is plausible using SPIO nanoparticles and a 16 echo spin echo MRI sequence.

4.1. SPIO concentration T_1 & T_2 calibration

Macs MicroBeads have not yet been characterized in literature. These specific MicroBeads were originally manufactured for magnetic cell separation and MRI analysis of these particles cannot be found. In order to assist with all subsequent MicroBead experimental designs, an SPIO concentration versus MRI effect calibration study was first performed. Multiple concentrations of SPIO nanoparticles were created in carrageenan gel and analyzed by the MRI. Calibration curves were created using the proton relaxation rates and the SPIO nanoparticle concentrations to the signal output that they produce in gel.

4.1.1. Materials and Methods

To determine the MRI contrast sensitivity of the MACS MicroBeads (SPIO molecules), concentrations of 1, 2.5, 5, 7.5, 10, 12.5, 15 & 25 μL/mL were created using varying increments of the MicroBeads added to 4mL of 1% carrageenan gel (ie. 100 μL of SPIO added to 4mL of gel makes a concentration of 25 μL /mL) and placed in vials to be measured with the MRI. A series of T_1 weighted images were acquired using standard inversion recovery sequences with TI = 100, 375, 500, 625, 750, 1000, 1130, 1250 and 1500 ms and TR = 5000 ms. A series of T_2 weighted images were acquired using multiple echo spin echo (MESE) imaging sequences with 16 different echo times starting from TE=15ms to TE=240 ms and TR = 5000 ms. The average and standard deviation of pixel intensity was measured using circular ROIs and the relaxation times (T_1 and T_2) and the relaxation rates ($1/T_1$ and $1/T_2$) were plotted versus iron concentration (μg/mL).

Both sequences had a resolution of 128 x 128 with a field of view (FOV) of 60 mm, a slice thickness of 3mm.

In parallel, another set of the same concentrations were dissolved in 9mL of double distilled water (ie. 225 μL of SPIO added to 9mL of ddH20 makes a concentration of 25 μL /mL) to determine the concentration of iron using a Jarrell-Ash inductively coupled argon plasma spectrometer (ICAP/ICP) operated by the Lakehead University Instrumentations laboratory. This result allows for a correlation between measured SPIO concentration and iron detected in parts per million (ppm = μg/mL).

For a more thorough examination of the MR properties of MACs nanoparticles the relaxation times were measured as a function of concentration of Macs MicroBeads at various field strengths of 1.5, 3, 7 and 11 Tesla. This study was performed in conjunction

with Peter Latta at the National Research council of Canada (NRC) Institute for Biodiagnostics (NRC-IBD) in Winnipeg, Manitoba.

4.1.2. Results

The increase in SPIO concentration results in a darkening of the area relative to the rest of the MRI output image as seen in Figure 12.

Figure 12: The effect due to the concentration of SPIO nanoparticles on MRI image. MRI output images corresponding to the first 7 data points. SPIO concentration increases from left to right.

The results from the ICP iron determination were plotted versus the concentration of known SPIO nanoparticles and are found in Figure 13. It is clear that the actual amount of iron present in the sample varies from the SPIO nanoparticle concentration. The correlation however is positive and linear which indicates that the iron concentration does increase as the concentration of SPIO nanoparticles increases. This result will aid in determining the actual MRI signal intensity effects due to iron concentration in the sample.

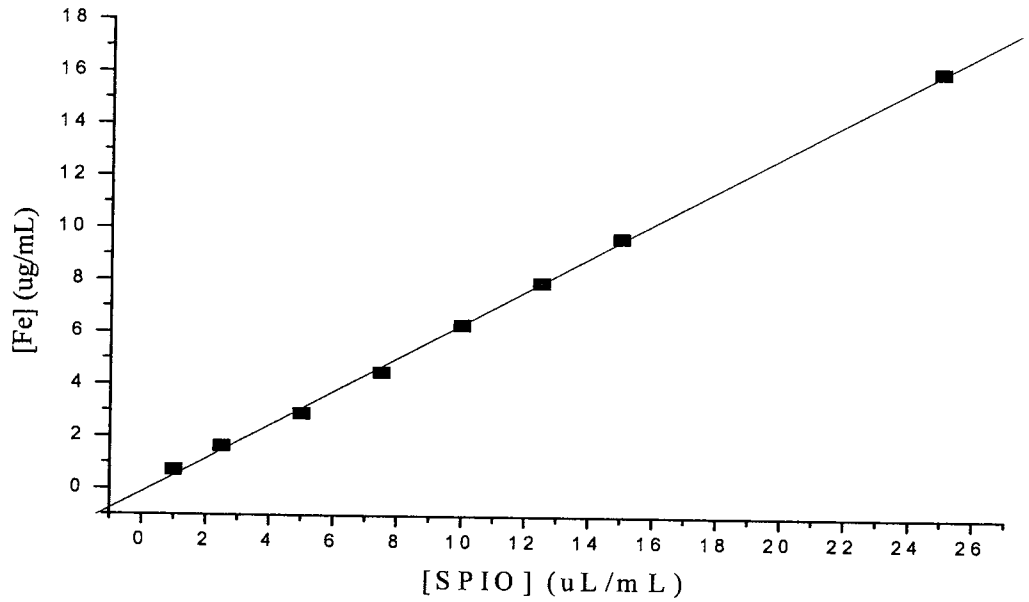

Figure 13: The relationship between iron content in the sample (measured with ICP) and the SPIO concentration measured experimentally. The equation of the line of best fit $y = -0.1371 + 0.648x$ ($R^2 = 0.99953$).

With this calibration curve (seen in Figure 13) and the results from the MRI, the relaxation times and relaxation rates were then plotted versus their corresponding iron concentrations. These relations can be found in Figures 14, 15, 16 & 17. Figures 14 & 15 show how the increase in iron concentration results in an exponential decay of T_1 & T_2. The equations of best fit are determined to be $y = 155.82 + 1263.27e^{-0.195x}$ for T_1 and $y = 31.52 + 1785.62e^{-1.285x}$ for T_2. In order to compare these exponential trends we will use the equation of exponential decay defined as follows:

$$y = y_o + A_o e^{-\lambda t}$$

Where y_o is the y-intercept, A_o is a constant and λ is the decay constant. According to this relation, the larger the decay constant the faster the dependent variable will decay due to less iron concentration present in the sample. It is obvious that T_2 decreases with a

much smaller concentration of iron required then T_1, which is displayed by the larger decay constant of 1.285 compared to 0.195 for T_1.

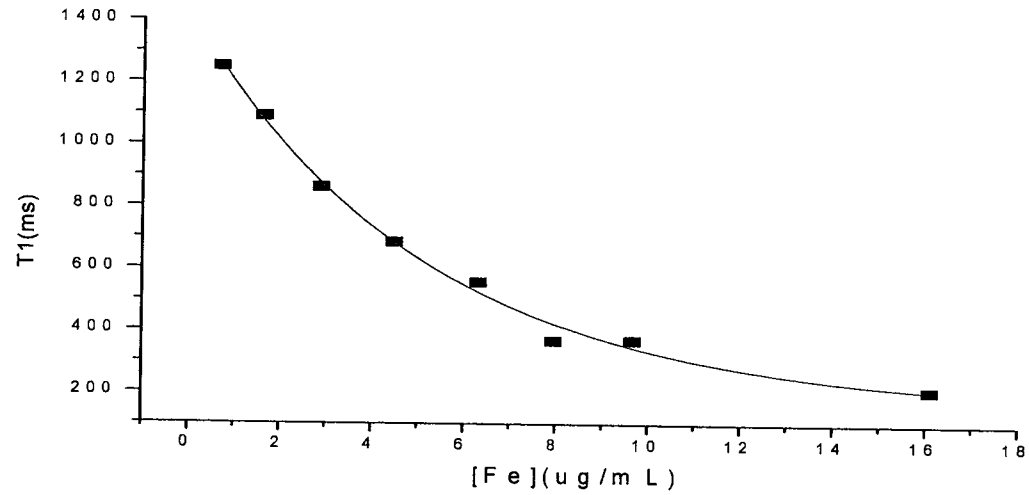

Figure 14: The relationship between the longitudinal relaxation time (T_1) and the concentration of iron present in the samples of Macs MicroBeads. The exponential curve fit was determined to be y = 155.82 + 1263.27exp(-0.195x)

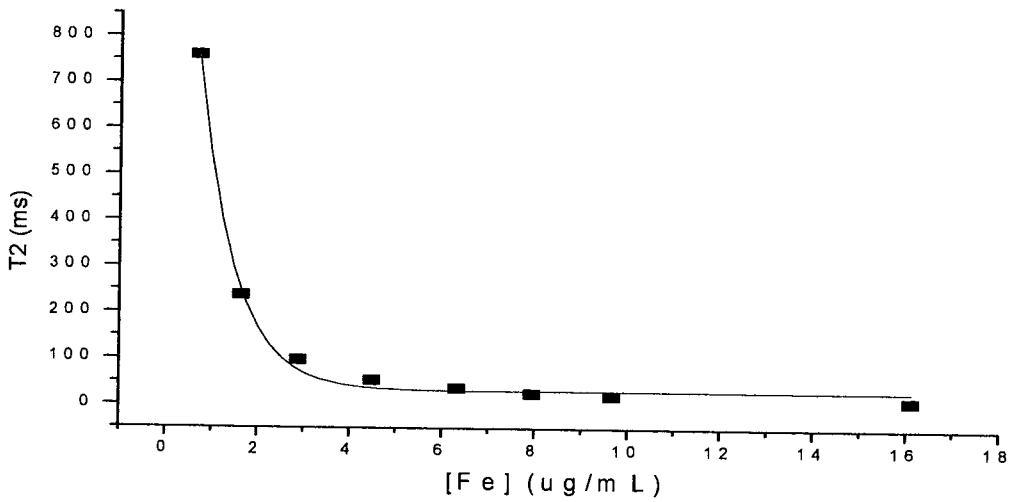

Figure 15: The relationship between the transverse relaxation time (T_2) and the concentration of iron present in the samples of Macs MicroBeads. The exponential curve fit was determined to be y = 31.52 + 1785.62exp(-1.285x)

Figure 16 and 17 display the relaxivity rates ($1/T_1$ & $1/T_2$) plotted versus their corresponding iron concentration due to the presence of SPIO nanoparticles. The relationship between R_1 and iron concentration is linear with the equation of the line of best fit being $y = 0.435 + 0.257x$ ($R^2 = 0.9897$). The relationship between R_2 and iron concentration was also linear with the equation of the line of best fit equal to $y = -4.275 + 5.254x$ ($R^2 = 0.9989$). Both relaxation rates (R_1 and R_2) increase with the concentration of iron present. The slope of the curves determine the change in relaxivity (ΔR_2) for every increase in Fe (ug/mL) present. This slope is otherwise known as the sensitivity of contrast that the increase in MACs MicroBeads (Fe) can provide. Since the transverse relaxation rate (R_2) increases more rapidly (with a slope value of 5.254) than the longitudinal relaxation rate (R_1) (slope value equals 0.257) it therefore provides a greater sensitivity to the SPIO nanoparticles.

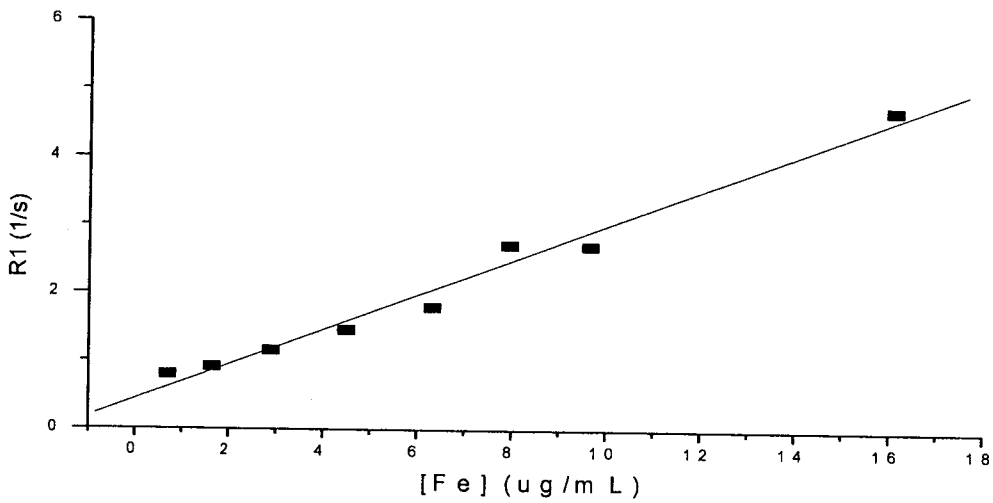

Figure 16: The relationship between the longitudinal relaxivity rate (R_1) and the concentration of iron in samples of SPIO nanoparticles. The equation of the line of best fit is $y = 0.435 + 0.257x$ ($R^2 = 0.9897$).

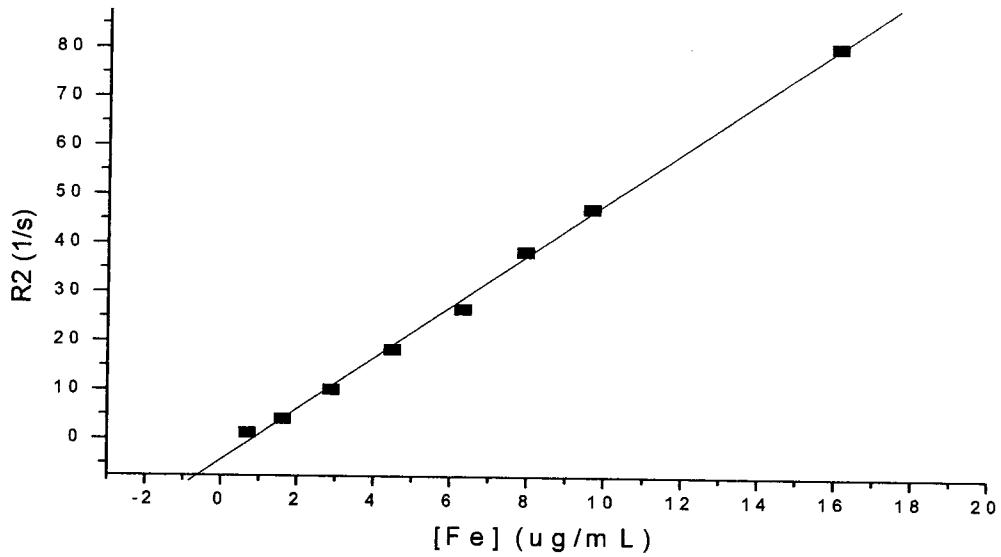

Figure 17: The relationship between the transverse relaxation rate (R_2) and the concentration of iron in samples of SPIO nanoparticles. The equation of the line of best fit is $y = -4.275 + 5.254x$ ($R^2 = 0.9989$)

The comparison of the same samples of SPIO concentrations in varying magnetic field strengths (found in Figures 18 and 19) also verify a positive correlation of R_1 and R_2 with iron concentration but, unlike R_1, R_2 is much less susceptible to these variations. This is demonstrated by the very slight variation in slopes between the magnetic field strengths of interest. The slopes for R_1 vs Fe range from 0.016 $mL \cdot ug^{-1}s^{-1}$ (when measured in the 11 T magnetic field) to 0.2495 $mL \cdot ug^{-1}s^{-1}$ (in the 1.5 T magnetic field). In comparison, the slopes for R_2 range from 3.553 $mL \cdot ug^{-1}s^{-1}$ (when measured in the 11 T magnetic field) to 5.254 $mL \cdot ug^{-1}s^{-1}$ (when measured in the 1.5 T magnetic field). The greatest range of relaxation rates (R_1 & R_2) allows for the best differentiation between concentrations of SPIO nanoparticles.

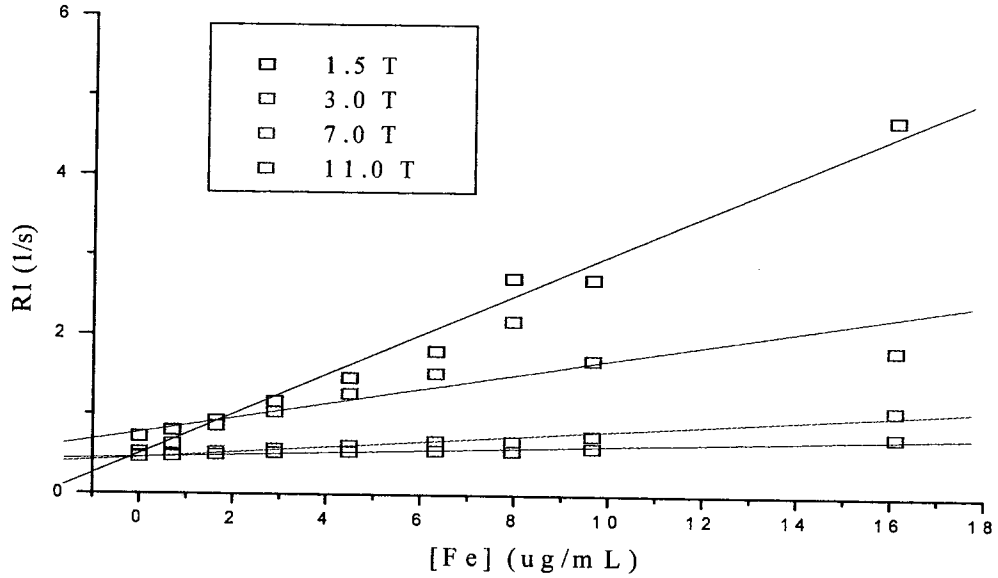

Figure 18: The Calibration Curve of R_1 vs Iron concentration at varying magnetic field strengths of 1.5, 3, 7 & 11 Tesla (NRC-IBD).

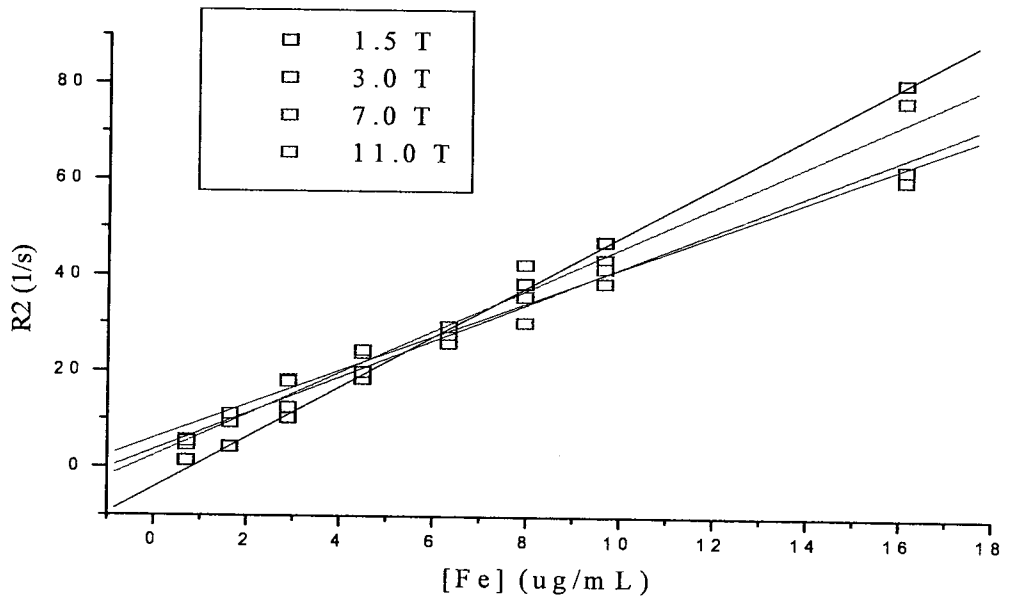

Figure 19: The Calibration Curve of R_2 vs Iron concentration at varying magnetic field strengths ranging from 1.5 to 11 Tesla (NRC-IBD)

4.1.3. Discussion

The SPIO nanoparticles of interest in this study are very powerful agents for reducing water proton transverse relaxation times. The increase in iron concentration results in a darkening of the area relative to the rest of the MRI output image displayed in Figure 12. It is very important for the contrast agent to be characterized by high relaxivity and to be detectable and functional at trace concentrations. The calibration curve found in Figure 13 allowed for a correlation between the experimental concentration of SPIO and the actual concentration of iron in the particles. It was clear from the results displayed in Figure 14 and 15 that the increase in iron concentration causes both T_1 and T_2 to decay exponentially. Comparing their exponential decay constants (λ) it is evident that Macs MicroBeads have the ability to decrease T_2 much more effectively (providing a greater contrast and more sensitivity) then T_1. T_2 had decreased to half of its original value after only 0.539 μg/mL of Fe was added whereas T_1 required 3.555 μg/mL. This effect is also evident when analyzing the inverse relaxation times (R_1 and R_2), which displayed positive linear correlations to the concentration of SPIO present in the samples shown in Figure 16 & 17. Bulte and colleagues also demonstrated a linear relationship between the R_2 relaxation rate and iron content[39]. The change in R_2 (ΔR_2) over SPIO concentration (5.254) is much greater than the change in R_1 (ΔR_1) (0.257) making the sensitivity of T_2 and R_2 to SPIO concentration more apparent. The greatest slope produced by the SPIO nanoparticles would provide the greatest sensitivity and its optimization is the main goal.

There was no significant difference between R_2 values calculated using various magnetic fields[43] thus verifying that R_2 is not as susceptible to changes in B_o. At this point, the greatest sensitivity to the SPIO particle of interest occurs at the 1.5T magnetic

field strength when investigating R_2 therefore this is the optimal environment to maximize the change in transverse relaxivity (ΔR_2) due to varying concentrations of SPIO for our investigations. This is also convenient since the clinical MRI that we have available to us is a 1.5T magnetic field strength. Therefore T_2 relaxation time MR imaging was used in all subsequent experiments.

In conclusion, the visual darkening of the output image and the quantified T_2 and R_2 values, together provide a method for determining SPIO nanoparticle concentration in a sample.

4.2. Feasibility Percent Apoptosis Gradient

Proton relaxation rate enhancements produced by MACS MicroBeads in carrageenan gels have produced a significant trend proportional to the relaxation rate (R_2) at a constant magnetic field strength of 1.5 Tesla. This preliminary investigation analyzes the behaviour of these particles when tagged to cells undergoing apoptosis.

4.2.1. Materials and Methods

HL-60 cells were counted, harvested and divided into two parts: one was transferred to a flask to be treated with etoposide (VP-16), and the other was left untreated. After time increments of 0, 2, 4, 6, 8 & 16 hrs, treated and untreated populations were analyzed by flow cytometry using Annexin V-FITC to quantify the amount of apoptosis. In parallel, treated and untreated populations were also placed in carrageenan gels at the appropriate time interval and analyzed with the MRI. T_2 weighted images were acquired using a 16 echo spin echo sequence with echo times ranging from 15ms to 240ms, TR= 5000 ms, resolution of 128 x 128, field of view (FOV) of 60 mm and a slice thickness of 3 mm. The test tubes were scanned and analyzed within 2-4 weeks of being made.

4.2.2. Results

The flow cytometry results indicated that there exists an increase in apoptotic cells as the treated time increased. Using the flow cytometry results and the measured transverse relaxation rate a plot of R_2 vs percent apoptosis was generated (see Figure 20). The data was fitted to a cubic polynomial trend (R^2= 0.9995) rather then a linear trend (R^2 = 0.9053).

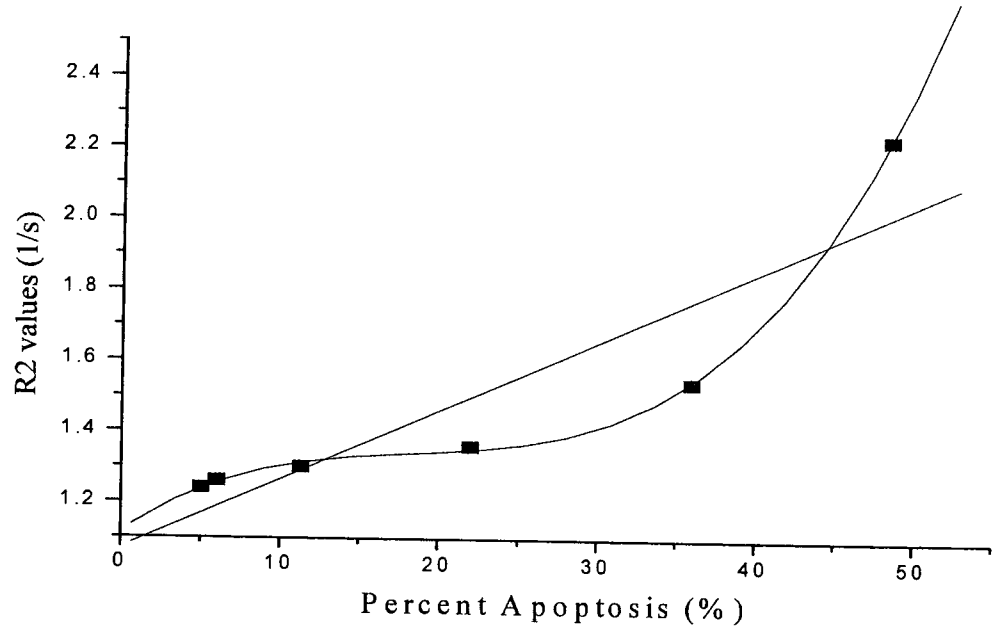

Figure 20: Correlation between inverse spin-spin relaxation time (R_2) and the level of percent apoptosis. Different level of apoptosis induced by exposing HL-60 cell samples to Etoposide for different times and then measured with flow cytometry. R_2 determined by MRI analysis of the same cell populations. Linear line of best fit equation is $y = 1.0706 + 0.0195x$ ($R^2 = 0.9053$), polynomial line of best fit equation is $y = 1.1145 + 0.0322x - 0.0016x^2 + 2.974x10\text{-}5x^3$ ($R^2 = 0.9995$).

4.2.3. Discussion

An important characteristic that the SPIO contrast agent should have is the efficiency to gain access to the target cells of interest. Cells undergoing apoptosis signal their neighbours by expressing phosphatidylserine (PS) on the external leaflet of the cell membrane[5]. Several proteins are known to bind to PS, of these, annexin V is best known[8]. Optimally up to eight annexin V moieties can bind to one exposed PS, which contributes to its efficiency as a cell label. MACS MicroBeads provided by Miltenyi Biotech have been FDA approved as well as come pre-conjugated to several ligands for easy use. The SPIO used in this study come pre-conjugated to annexin V and thus will provide a mechanism to label cells undergoing apoptosis.

Initially, apoptosis was induced in HL-60 cells using the chemotherapy drug etoposide (VP-16) over various treatment times, and then tagged with MACS MicroBeads. After the longest time of etoposide treatment of 16 h, only >50% apoptosis was induced. This method of induction of apoptosis does not have the capability of inducing 100 percent apoptosis that is required within a reasonable time frame. Therefore, a new method of treatment was analyzed.

The preliminary results (shown in Figure 20) show a strong correlation between R_2 and percentage of cells that were apoptotic. This relationship has been analyzed using a third order polynomial trend fitting and a linear trend fitting. The initial hypothesis was that the relationship would be a linear one similar to how the SPIO nanoparticles behave without being tagged to cells but this does not seem to be the case (as seen in figure 20). After the feasibility study, we can conclude that the results need to be analyzed further to examine the details of this relationship between R_2 and percent apoptosis. The following experiments are designed to optimize experimental parameters in order determine the correct relationship between R_2 and percent apoptosis and also establish the sensitivity and the precision of this detection technique.

4.3. *Detection of 100% apoptosis with PS bound SPIO nanoparticles*

In order to perform a dilution study to generate multiple populations of known levels of apoptosis that range from zero to 100 percent, a technique that is capable of inducing 100% apoptosis was required. Since etoposide was unable to produce that level of apoptosis (in a reasonable time frame), heat shock was then analyzed. Once 100 percent apoptosis is produced we then compared its MRI output contrast to that of healthy cells when tagged with SPIO nanoparticles to determine if they are differentiable using MRI.

4.3.1. Materials and Methods

HL-60 cells were counted, harvested and divided into two parts: one was transferred to a flask to be treated with heat shock, and the other was left untreated. Treated and untreated populations were analyzed by flow cytometry using Annexin V-FITC to quantify the amount of apoptosis. In parallel, treated and untreated populations were tagged with MACS MicroBeads, placed in 1% carrageenan gel at a concentration of 200 x 10^6 cells/mL and analyzed with the MRI. T_2 weighted images were acquired using a 16 echo spin echo sequence with echo times ranging from 15ms to 240ms, TR= 5000 ms, resolution of 128 x 128, FOV of 60mm and a slice thickness of 3 mm. The plates were analyzed by the MRI within 2-4 weeks of being plated.

4.3.2. Results

According to the results from flow cytometry shown in Figure 21 A & B, HL-60 cells treated with heat shock result in the majority of cells to be annexin V positive (upper region), while a population left untreated showed the majority of cells to be annexin V negative (lower region). The more counts of the fluorescence parameter (FL1-H)

indicates more annexin V-FITC and therefore more cells are annexin V positive, and the population will appear in the upper region of the plot in Figure 21 B. In this case, 96% apoptosis was induced in HL-60 cells using heat shock, while the untreated remained at 4%. Both treated and untreated cells were tagged with SPIO nanoparticles and the result demonstrated that ~100% apoptotic cells tagged by PS targeted SPIO nanoparticles had a smaller T_2 value (78ms) than healthy cells (150ms)(see Figure 21C) and appeared less intense in the MRI image (see Figure 21 D,E).

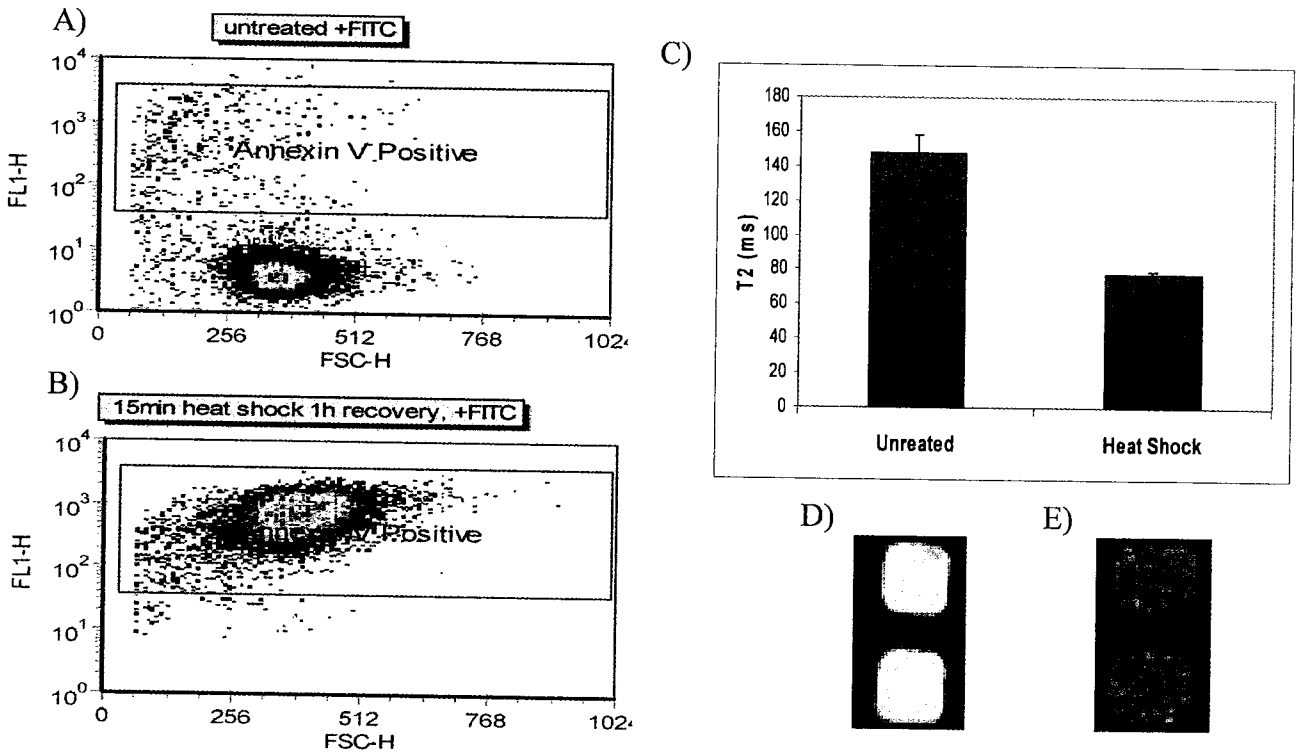

Figure 21: Feasibility Investigation. HL-60 cells heat shocked to induce nearly 100% apoptosis. A) Flow cytometry data for untreated cell population, B) Flow cytometry data for treated cell population, C) T_2 relaxation times for untreated and heat shocked populations, D) & E) T_2 MRI images for untreated and heat shocked populations respectively.

4.3.3. Discussion

Analysis of the flow cytometry data made the quantification of annexin V positive (apoptotic) HL-60 cells possible (see Figure 21A, B). Heat shock was capable of inducing approximately 100% apoptosis in only 15 min (exposure) and 1 h recovery. Correlating the flow cytometry results to the T_2 measurement for treated and untreated cells clearly indicated a shorter T_2 relaxation for 100% apoptotic cells (see Figure 21C) and appear darker in an MRI output image (see Figure 21D &E). This result proves that apoptotic cells tagged by PS targeted SPIO nanoparticles will have a smaller T_2 value (78ms) than healthy cells (150ms) and appear less intense in a T_2 MRI image. In order to quantify the degree of apoptotic damage in treated HL-60 cells there were minor details to work out in the procedure. First of all, the concentration of cells which displays the best MRI contrast was determined and second, a dilution technique was performed using treated and untreated cells to create increments of apoptotic populations between 0 and 100%. The concentration of cells used (200×10^6 cells/mL) turned out to be a too large to be suspended in such a small volume of gel and so an optimal concentration was also determined.

4.4. The effect of cell concentration on sensitivity of apoptotic percent measurement

In order to generate the greatest sensitivity as well as the greatest differentiation between tagged and untagged cells, the next step was to optimize the concentration of cells used.

4.4.1. Materials and Methods

After an appropriate incubation time, HL-60 cells were counted, harvested and divided into two parts: one was transferred to a flask to be heat shocked (treated) to achieve 100% apoptosis, and the other was left untreated. A known concentration of treated cells was diluted to the approximate volumes required to create concentrations of 5, 10, 20, 30, 40, 60 & 120 x 10^6 cells/mL. These populations were then tagged with MACS MicroBeads (Miltenyi Biotech), suspended in gel and placed in the 384-well microplate as previously stated in the general techniques. T_2 weighted images were acquired using a 16 echo spin echo sequence with echo times ranging from 15ms to 240ms, TR= 5000 ms, resolution of 128 x 128, FOV of 60mm and a slice thickness of 3 mm. The plates were analyzed by the MRI within 2-4 weeks of being plated.

4.4.2. Results

The variation of R_2 with concentration was determined and displayed in Figure 22 for both treated/tagged and untagged/untagged populations and the increase in R_2 per unit of concentration of cells. The ΔR_2 value was calculated by taking the difference between treated/tagged R_2 values and untreated/untagged R_2 values at each concentration of cells. As the concentration of cells increases so does the R_2 value for both populations. The difference between the two populations (sensitivity) increases as the concentration of

cells increases as shown in Figure 23. Therefore a higher concentration of cells will create a greater difference in ΔR_2 and thus increasing the sensitivity of this technique

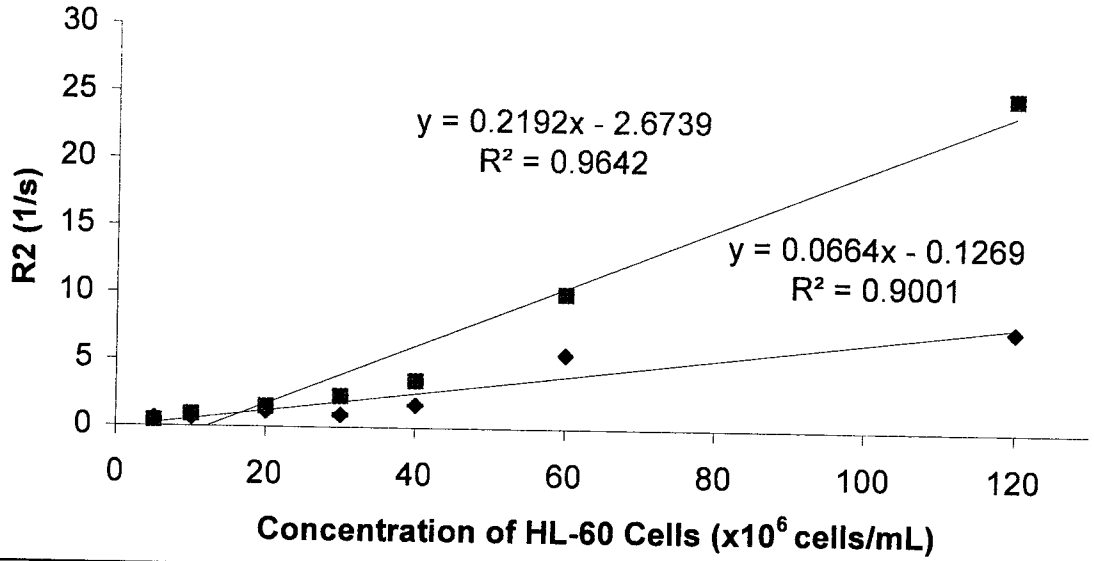

Figure 22: R_2 vs concentration of 100% apoptotic cells (treated/tagged)(pink) and untreated/untagged cells (navy) at various cell concentrations. R_2 determined by MRI analysis.

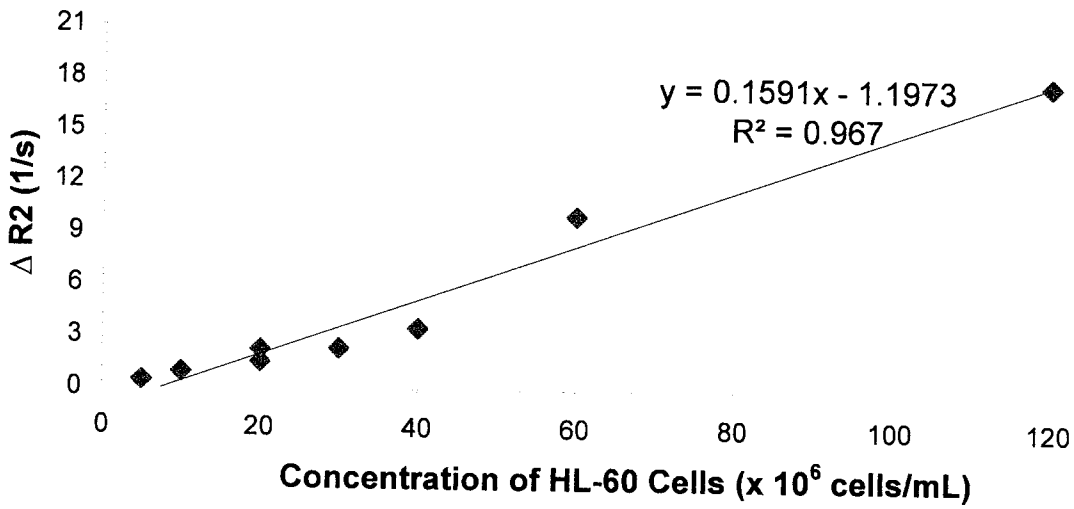

Figure 23: The difference in relaxivity rate (R_2) between treated/tagged and untreated/untagged cells as the concentration of cells varies. R_2 determined by MRI analysis. Regression line displayed.

4.4.3. Discussion

Analysis of various cell concentrations shown in Figures 22 & 23 illustrate that the greater the cell concentration the greater the change in R_2 between treated/tagged and untreated/untagged cells. A positive correlation was suspected since literature had previously found a linear result for gliosarcoma cells and lymphocytes when tagged with SPIO nanoparticles[43]. The greater the ΔR_2 value the greater the differentiation will be between treated/tagged and untreated/untagged cells in sensitivity. This is also shown in Figure 23 with the positive linear correlation ($R^2 = 0.967$) between ΔR_2 and concentration of cells present. The result in Figure 22 suggests that the larger the cell concentration the greater the MR contrast and the differentiation between treated and untreated cells in sensitivity (ΔR_2). A greater ΔR_2 over a range of cell concentration or degree of apoptotic damage will allow a greater differentiation /sensitivity using R_2 in both cases. Maximizing ΔR_2 increases the sensitivity of this MR technique and thus was the goal throughout the experiment. Kuhlpeter and colleagues[44] determined the slope of the R_2 vs concentration of cells curve to be 1.9×10^{-5} mL/cells • s for human lung carcinoma cells which differs greatly compared to our result of 2.192×10^{-7} mL/cells • s for HL60 cells. This result could be expected according to Rad et al[43] who determined that regression lines differ depending on cell types.

From the results in Figures 22 & 23 we can summarize that the greatest amount of cells would have the advantage of having a greater differentiation between treated/tagged and untreated/untagged cells. On the other hand, dealing with too large of a cell concentration has proven to be a disadvantage. In the preliminary apoptosis gradient study (section 4.2) it was determined that 200×10^6 cells created too large of a cell pellet

to be resuspended in 100uL of gel without difficulty. Large concentrations (150-200 x 10^6 cells/mL) are difficult to suspend in the small volume of gel used and could result in potential human error and inhomogenieties in our samples. Therefore, a large concentration of ~120 x 10^6 cells/mL should be examined for the next experiment. This concentration may provide the significant contrast required to perform the percent apoptosis gradient while minimizing any potential human error that may occur.

Having optimized the concentration of cells for sufficient MR contrast, and having the means of inducing ~100% apoptosis, the percent apoptosis gradient can now be performed, reproduced and analyzed.

4.5. *Percent Apoptosis Gradient using heat shock*

Having the means to induce 100 percent apoptosis using heat shock and having established an optimal concentration of cells (120 x 10^6 cells/mL) to provide sufficient MR contrast we were then able to create an apoptosis gradient that examines the relationship between the transverse relaxation rate and the percent apoptosis present in our samples.

4.5.1. Materials and Methods

Using the experimental result from the concentration gradient, the first analysis of the apoptosis gradient used a concentration of 120 x 10^6 cells/mL. After an appropriate incubation time, HL-60 cells were counted, harvested and divided into two parts: one was transferred to a flask to be treated to achieve 100% apoptosis, and the other was left untreated. In order to generate cell populations consisting of varying percentages of apoptotic cells, treated cells were mixed with untreated cells at known concentrations. Figure 24 gives an overview of the detection methods involving the parallel study of MRI and flow cytometry used in order to detect and quantify early stage apoptosis. Dilution was performed to give nominal apoptosis of 0, 20, 40, 60, 80 & 100%. Once the apoptotic cell populations were prepared, the samples were then again harvested and divided into two parts: the first was transferred to flow tubes to be stained with annexin-V-FITC to quantify the amount of apoptosis using flow cytometry and the second was stained with Annexin V MACS MicroBeads to determine the signal intensity from the MRI (see Figure 24). MRI parameters TE = 10 - 73.7ms, TR = 5000 ms and a FOV = 80 mm. The plates were analyzed by the MRI within 2-4 weeks of being plated.

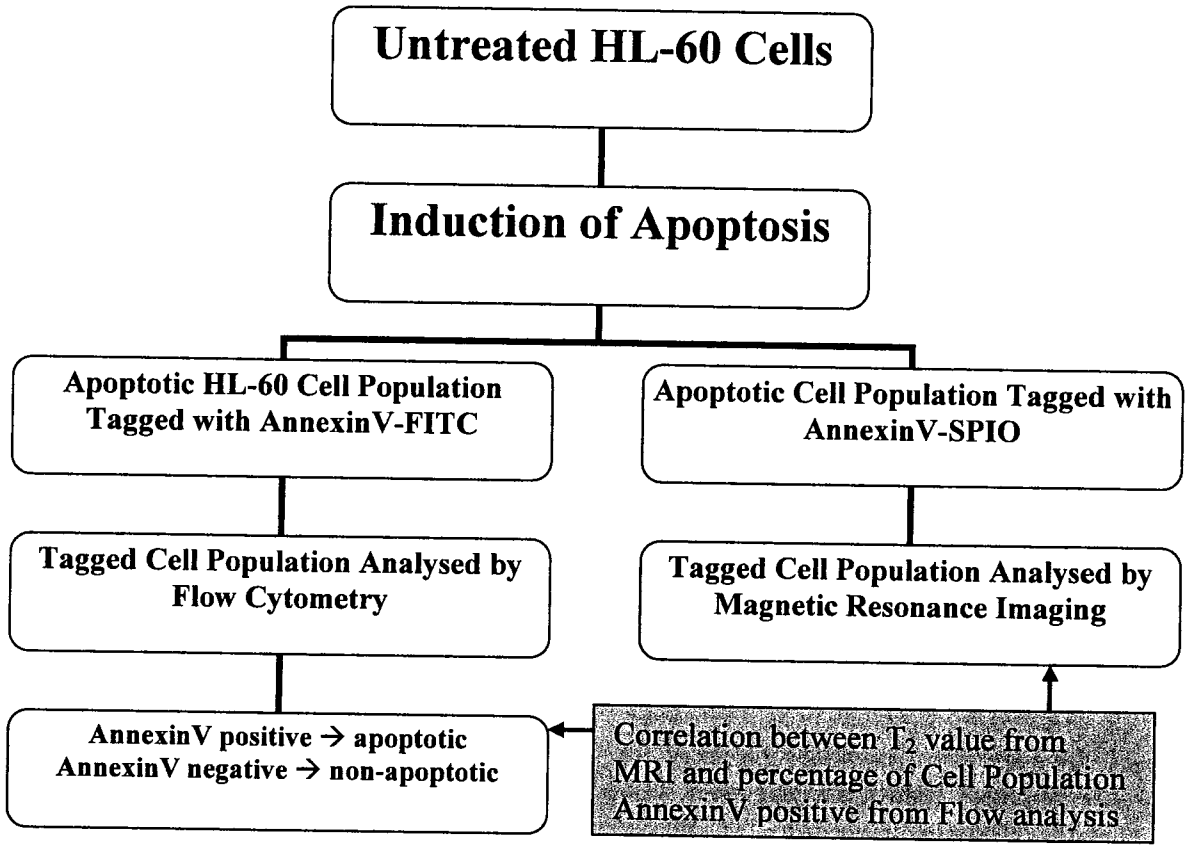

Figure 24: Detection of early stage apoptosis. MRI and flow cytometry analysis are carried out in parallel on induced apoptotic cell populations. Flow cytometry is used to determine the percentage of the given cell population that was apoptotic using fluorescent molecules tagged to PS. This value was correlated with T_2 from an MRI of the same population using SPIO molecules targeted to PS.

4.5.2. Results

Heat shock to achieve ~100% apoptosis (99.36%) now gives the ability to generate different levels of apoptosis using a dilution technique mixing treated and untreated cells. All results were benchmarked relative to controls from the FITC assay shown in Figure 25 and Table 2. It is important to know that the brighter the specific fluorescence events will yield a higher pulse height and thus a higher channel number when displayed on a histogram. The total number of cells in the second marker (M2) histogram quantifies the

amount of annexin V positive cells since a brighter fluorescence indicates more apoptotic cells. Table 2 displays the results of total apoptosis in each sample, which vary each time the experiment is completed. Using flow cytometry results in parallel with MRI analysis the inverse T_2 relaxation time of an apoptotic cell population tagged with SPIO nanoparticles was correlated to the percentage of that population that is apoptotic (see Figure 26). R_2 values from the healthy cells (8.88%) were significantly increased from $2.157 \pm 0.383\ s^{-1}$ to $7.503 \pm 0.358\ s^{-1}$ due to incubation with annexin V MicroBeads. However, apoptotic cells (99.36%) that had been incubated with annexin V MicroBeads showed a more dominant increase in R_2 values from $2.419 \pm 0.144\ s^{-1}$ to $24.876 \pm 1.238\ s^{-1}$. The line of best fit had an equation of $y = 0.16072x + 8.5602$ ($R^2 = 0.8275$) and the best polynomial fit was a third order equation of $y = 1.657 + 0.790x - 0.014x^2 + 8.143E^5x^3$ ($R^2 = 0.99817$).

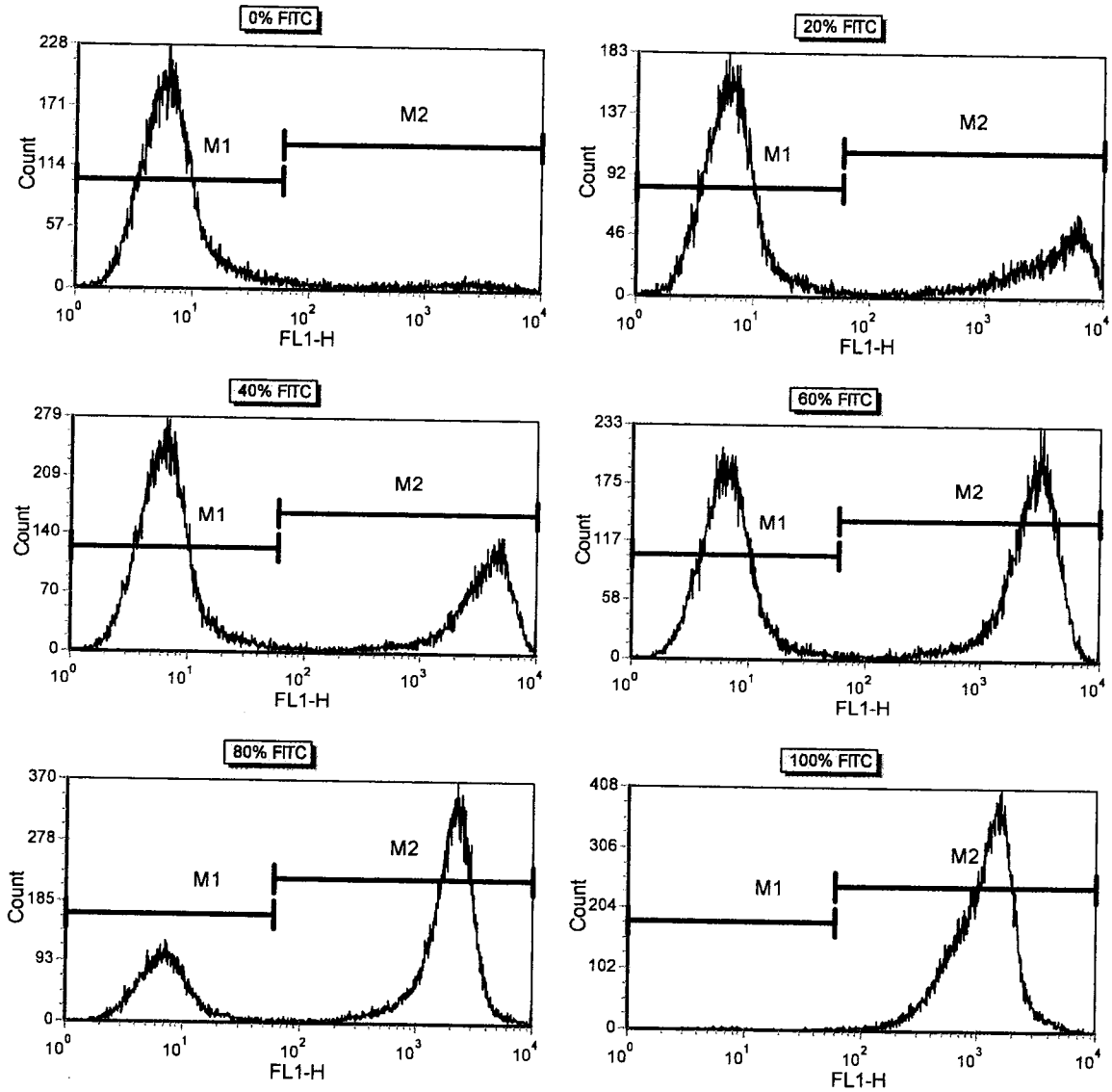

Figure 25: Flow cytometry results labelled according to experimental percentage values to be achieved. The data collection histograms depicting the increase in annexin V positive cells (increase in M2 marker)

Table 2: The flow cytometry results obtained from histogram analysis.

Experimental % value	# of events (M1)	# of events (M2)	% of all cells annexin V (-)	% of all cells annexin V (+)
0	27336	2664	91.12	8.88
20	21561	8439	71.87	28.13
40	33081	16919	66.16	33.84
60	25404	24596	50.81	49.19
80	13945	36055	27.89	72.11
100	322	49678	0.64	99.36

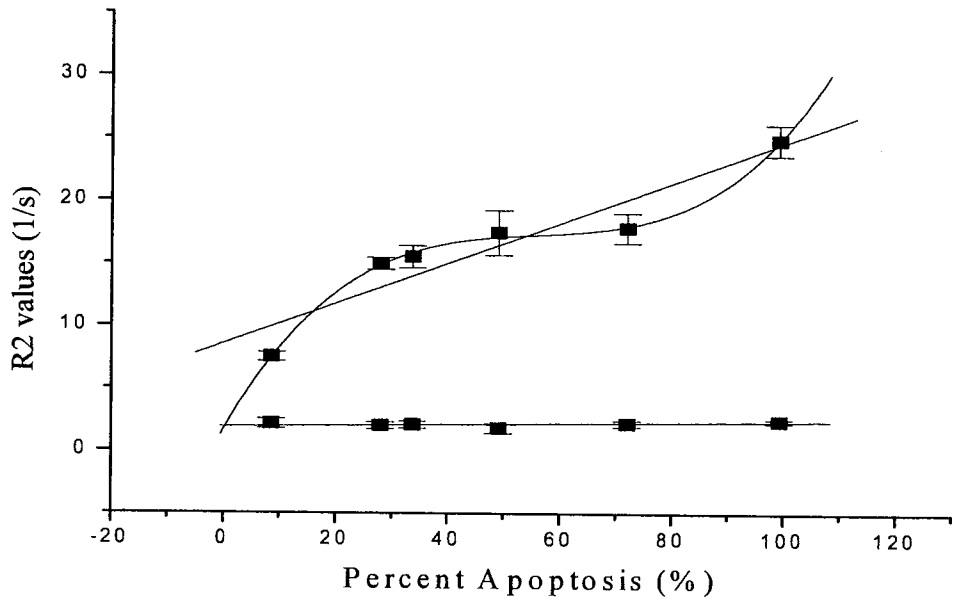

Figure 26: The correlation between the spin-spin relaxivity rate (R_2) and the percent of apoptosis in tagged cells at a concentration of 120 x 10^6 cells/mL. R_2 determined by MRI analysis. Linear fit and polynomial fit displayed for tagged population. Line of best fit equation: $y = 0.16072x + 8.5602$, $R^2 = 0.94005$. Polynomial fit equation: $y = 1.657 + 0.790x - 0.014x^2 + 8.143\ E^{-5}x^3$, $R^2 = 0.99817$, Line of best fit for untagged population $y = 1.9 + 0.005x$, $R^2 = 0.8275$

4.5.3. Discussion

This parallel approach using flow cytometry and MRI allowed us to use a well established technique to characterize the emerging technique of molecular MRI. Annexin V conjugated to a superparamagnetic complex has been previously used for apoptosis detection by MRI [38]. The goal in this case was to find the relationship that best predicts y (percent apoptosis) from x (R_2 or ΔR_2). The result supports a model with a third order polynomial fit ($R^2 = 0.998$) rather then a linear fit ($R^2 = 0.940$). An R^2 of 0.998 for the polynomial fit and 0.940 for the linear fit implies that 99.8 % of the y variable is explained by the x in a polynomial fit and only 94% in a linear fit. This result is actually in disagreement with literature that has predicted a linear fit for R_2 and SPIO nanoparticles bound to apoptotic cells [41, 43]. Sosnovik[41] determined a linear relationship between R_2* and degree of apoptosis and Rad[43] determined a linear relationship between R_2 and degree of apoptosis using different types of SPIO nanoparticles, different sequences and parameters and different cell lines. This apparent lack of agreement with the previously reported linear relationship prompted us to evaluate the reproducibility of our results.

There were still too many cells to suspend in the small volume of gel in the microplate and to avoid inhomogenieties a concentration 60 x 10^6 cells/mL will be used in the reproducibility study. This concentration of cells will provide sufficient contrast according to Figure 22 and will make cell suspension simpler thus avoiding any potential systematic errors.

4.6. Reproducibility Study: Percent Apoptosis Gradient

The feasibility study in section 4.5 gave the unexpected third order polynomial fit. In order to confirm this result, we performed a reproducibility study repeating the experiment 6 times.

4.6.1. Materials and Methods

Due to problems discussed in section 4.5, we used a concentration of 60 x 10^6 cells/mL for the following reproducibility study. As in the percent apoptosis study (section 4.5) for each reproducibility study, 6 different percent apoptosis values were achieved ranging from untreated to completely treated (100%). Three cell populations where analyzed in the MRI: tagged with annexin V-SPIO, tagged with basic SPIO and untagged cells. It must be noted that during the heat shock treatment in reproducibility study #4 the temperature did not reach the required temperature of 65°C. This resulted in less than 100% apoptosis being induced and therefore the percentages created in the dilution study only range from 0-45% (see Figure 30).

4.6.2. Results

Figures 27-32 show the results of the 6 reproducibility experiments performed. The results of reproducibility study #1 are shown in Figure 27. In this study a third degree polynomial relationship ($R^2 = 0.999$) was established between apoptotic cell death percentage and the spin-spin relaxivity rate (R_2). For cells tagged with Macs MicroBeads (annexin V-SPIO) the relationship is determined to be $y = 1.074 + 0.166x - 0.001x^2 + 4.464E^{-6}x^3$. For cells tagged with basic microbeads (SPIO alone) the relationship is determined to be $y = 1.060 + 0.014x - 3.701E^{-4}x^2 + 2.302E^{-6}x^3$. For untagged cells the

relationship is determined to be $y = 1.463 - 0.019x + 2.696E^{-4}x^2 - 1.201E^{-6}x^3$. The R_2 values range from $2.727 \pm 0.1307\ s^{-1}$ to $7.364 \pm 0.3308\ s^{-1}$. It is important to note that the SPIO nanoparticles pre-bound to annexin V have significantly higher R_2 values than both control populations (see Figure 27). Since tagging with basic SPIO nanoparticles does not significantly affect the R_2 values our rinsing techniques are proven to be successful in riding all excess SPIO and so basic SPIO will no longer be of interest in the next reproducibility studies.

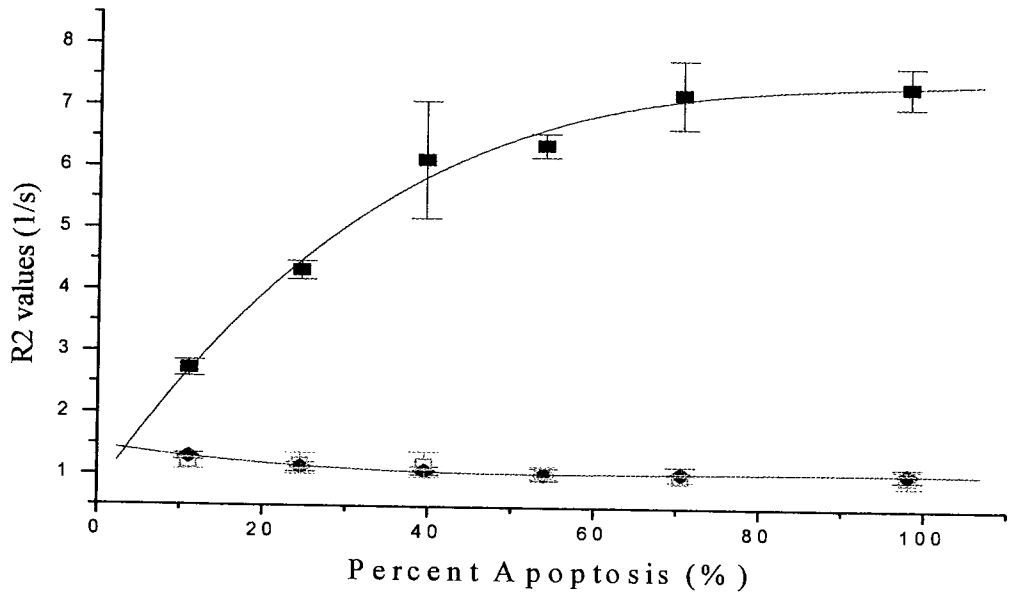

Figure 27: Reproducibility study #1. R_2 vs. Percent Apoptosis. The correlation between the spin-spin relaxivity rate (R_2) and the percent of apoptosis in cells tagged with annexin V-SPIO (blue), cells tagged with basic microbeads (cyan) and untagged cells (magenta) at a concentration of 60×10^6 cells/mL. R_2 determined by MRI analysis. Third degree polynomial fit lines displayed for both tagged and untagged populations. Polynomial fit equation for cells tagged with annexin V-SPIO: $y = 1.074 + 0.166x - 0.002x^2 + 4.464E^{-6}x^3$ (R^2=0.999), for cells tagged with basic SPIO: $y = 1.080 + 0.012x - 3.397E^{-4}x^2 + 2.143E^{-6}x^3$ (R^2=0.9926), for untagged cells: $y = 1.463 - 0.019x + 2.724E^{-4}x^2 - 1.228E^{-6}x^3$ (R^2=0.992).

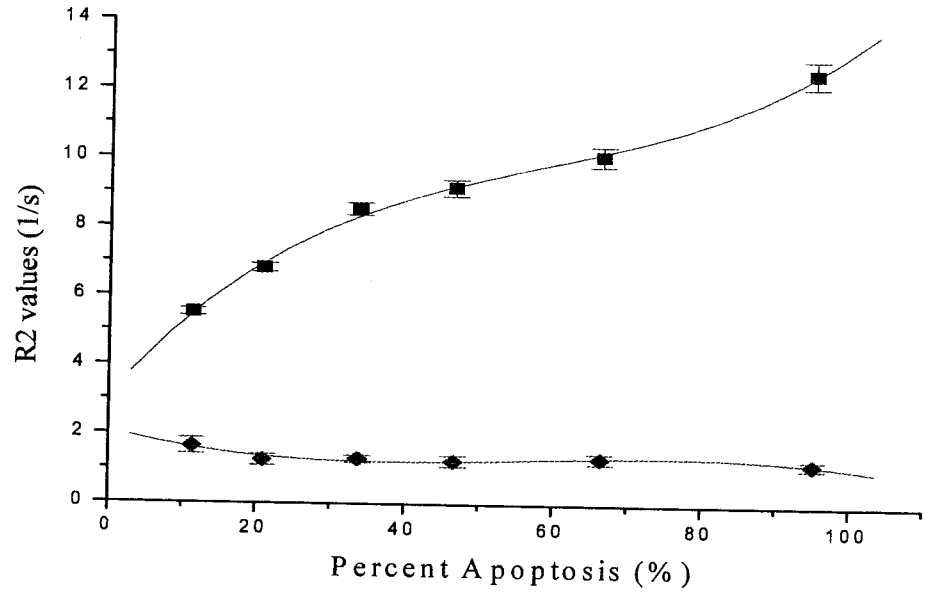

Figure 28: Reproducibility study #2. R_2 vs. Percent Apoptosis. The correlation between the spin-spin relaxivity rate (R_2) and the percent of apoptosis in tagged and untagged cells at a concentration of 60 x 10^6 cells/mL. R_2 determined by MRI analysis. Third degree polynomial fit lines displayed for both tagged and untagged populations. Polynomial fit equation for tagged cells: $y = 2.849 + 0.271x - 0.004x^2 + 2.293E^{-5}x^3$, ($R^2 = 0.9978$) for untagged cells: $y = 2.088 - 0.054 + 0.001\ x^2 - 6.138E^{-6}x^3$ ($R^2 = 0.85329$).

Reproducibility studies #2, #3, #4, #5 and #6 (see Figures 28, 29, 30, 31 & 32) have similar relationships and all seem to follow a similar third order polynomial trend. Study #4 shown in Figure has the most atypical shape compared to the others since it's range of percent apoptosis is limited to only >45% due to lower temperature during heat shock procedure resulting in less apoptotic percentages.

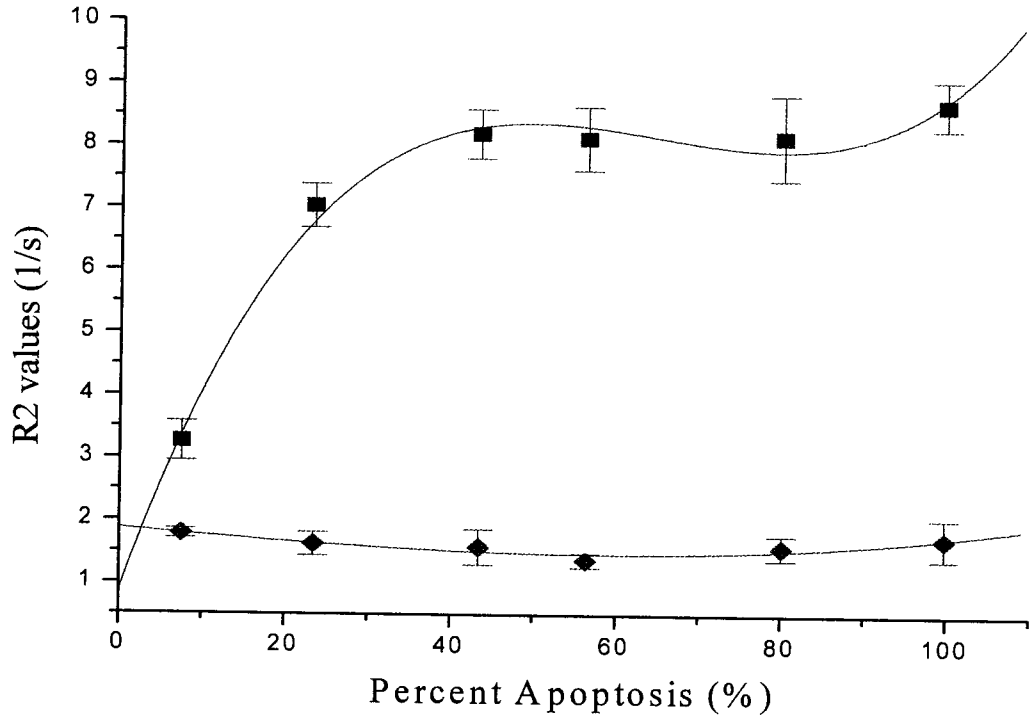

Figure 29: Reproducibility study #3. R_2 vs. Percent Apoptosis. The correlation between the spin-spin relaxivity rate (R_2) and the percent of apoptosis in tagged and untagged cells at a concentration of 60 x 10^6 cells/mL. R_2 determined by MRI analysis. Third degree polynomial fit equation for tagged cells: $y = 0.866 + 0.381x - 0.006x^2 + 3.191E^{-5}x^3$ ($R^2 = 0.9915$), for untagged cells: $y = 1.870 - 0.011x + 4.172E^{-4}x^2 + 5.792E^{-7}x^3$ ($R^2 = 0.8205$)

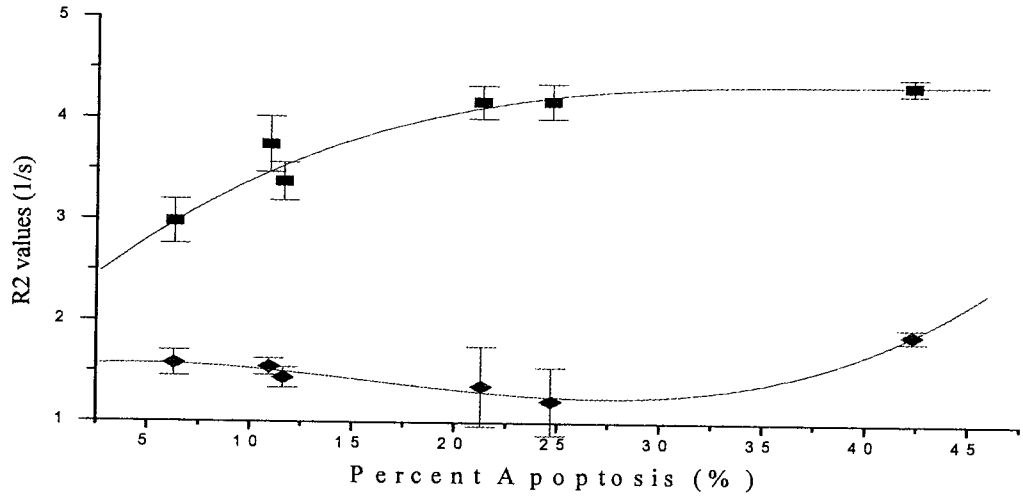

Figure 30: Reproducibility study #4. R_2 vs. Percent Apoptosis. The correlation between the spin-spin relaxivity rate (R_2) and the percent of apoptosis in tagged and untagged cells at a concentration of 60 x 10^6 cells/mL. R_2 determined by MRI analysis. Third degree polynomial fit equation for tagged cells: $y = 1.882 + 0.213x - 0.006x^2 + 6.663E^{-5}x^3$ ($R^2 = 0.9915$), for untagged cells: $y = 1.870 - 0.011x + 4.172E^{-3}x^2 + 5.792E^{-5}x^3$ ($R^2 = 0.8205$)

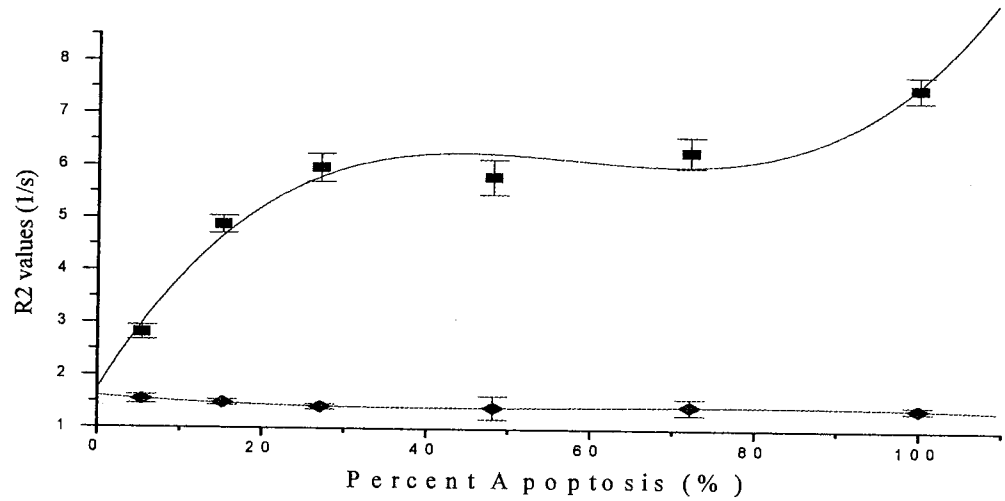

Figure 31: Reproducibility study #5. R_2 vs. Percent Apoptosis. The correlation between the spin-spin relaxivity rate (R_2) and the percent of apoptosis in tagged and untagged cells at a concentration of 60 x 10^6 cells/mL. R_2 determined by MRI analysis. Third degree polynomial fit equation for tagged cells: $y = 1.734 + 0.257x - 0.005x^2 + 2.72E^{-5}x^3$ ($R^2 = 0.9692$), for untagged cells: $y = 1.591 - 0.011x + 2.035E^{-4}x^2 - 1.093E^{-6}x^3$ ($R^2 = 0.986$)

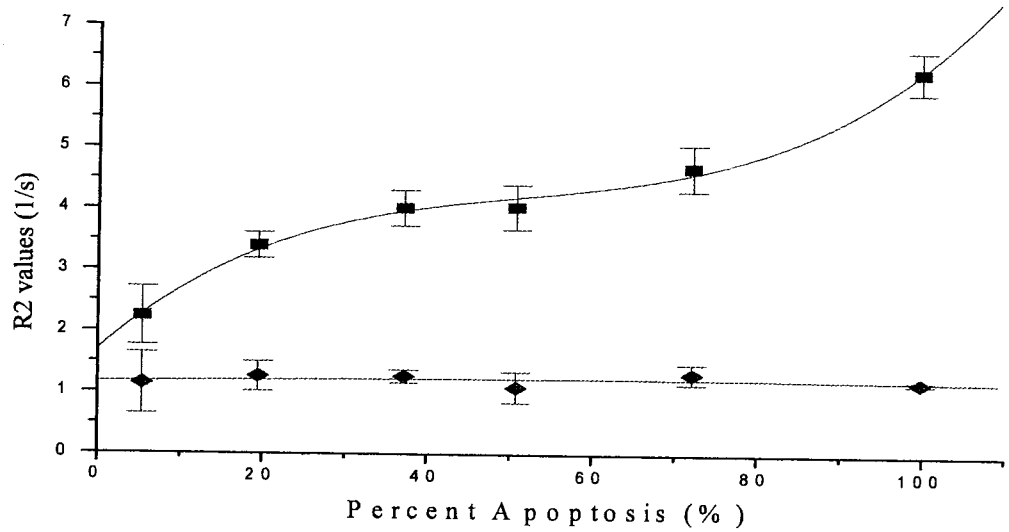

Figure 32: Reproducibility study #6. R_2 vs. Percent Apoptosis. The correlation between the spin-spin relaxivity rate (R_2) and the percent of apoptosis in tagged and untagged cells at a concentration of 60 x 10^6 cells/mL. R_2 determined by MRI analysis. Third degree polynomial fit equation for tagged cells: $y = 1.701 + 0.118x - 0.002x^2 + 1.30E^{-5}x^3$ ($R^2 = 0.9953$), for untagged cells: $y = 1.171 + 0.002x - 1.894E^{-5}x^2 + 1.640E^{-8}x^3$ ($R^2 = 0.055$)

A summary of the reproducibility studies can be found in Table 3. For further comparison, all of the studies were plotted on the same graph (seen in Figure 33) to analyze the curves all together. For cells tagged with Macs MicroBeads (annexin V-SPIO) at a concentration of 60 x 10^6 cells/mL the average relationship is determined to be $y = 1.945 + 0.187x - 0.002\ x^2 + 1.161E^{-5}\ x^3$ ($R^2 = 0.523$) for all reproducibility studies. For untagged cells the average relationship is determined to be $y = 1.570 - 0.013x + 1.918E^{-4}x^2 - 8.8680E^{-7}x^3$ ($R^2 = 0.085$). The functional coefficient for tagged cells implies that R_2 and percent apoptosis show a very poor correlation (52.3%) over multiple trials.

Table 3: Comparison of polynomial analysis for reproducibility studies #1-6 (tagged cells). Third degree polynomial defined by the general equation $y = A + Bx + Cx^2 + Dx^3$. Note: The upper range average for R_2 does not include study #4 since it does not cover a hundred percent apoptosis.

Study #	A	B	C	D	Lower Range of R_2	Upper Range of R_2	R^2
1	1.074	0.166	-0.001	4.46E-06	2.727 +/- 0.130	7.364 +/- 0.331	0.9986
2	2.849	0.271	-0.004	2.29E-05	5.521 +/- 0.102	10.395 +/- 0.249	0.9978
3	0.866	0.381	-0.006	3.19E-05	3.265 +/- 0.316	8.679 +/- 0.392	0.9915
4	1.882	0.213	-0.006	6.66E-05	2.978 +/- 0.219	4.341 +/- 0.082	0.9344
5	1.734	0.257	-0.005	2.72E-05	2.804 +/- 0.140	7.530 +/- 0.244	0.9692
6	1.701	0.118	-0.002	1.30E-05	2.243 +/ 0.476	6.263 +/- 0.315	0.9953
Average	1.6843	0.2343	-0.004	2.76757E-05	3.256	8.046	
St. Dev	0.6986	0.0917	0.0021	2.15091E-05	1.159	1.568	

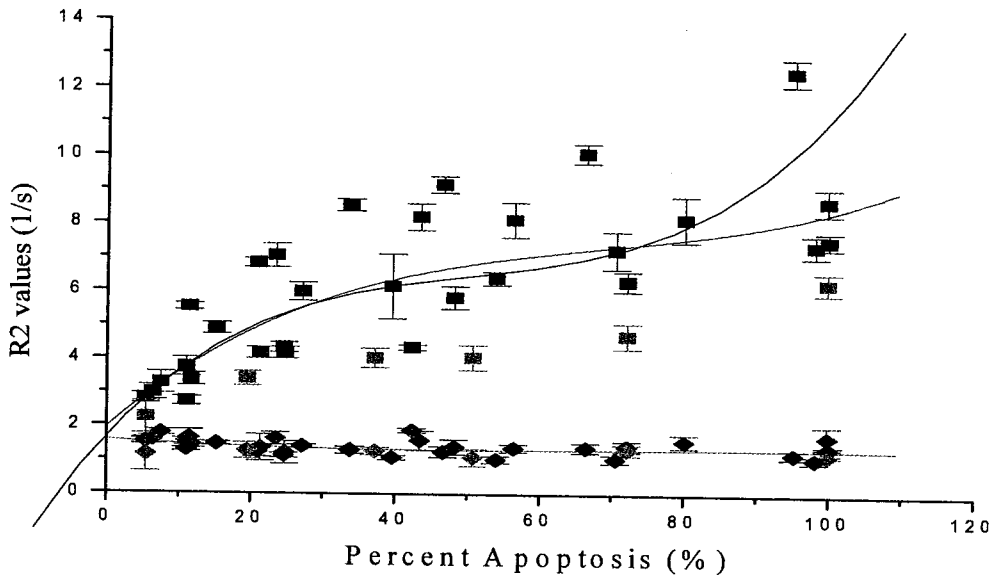

Figure 33: The relationship comparison between the spin-spin relaxivity rate (R_2) and the percent of apoptosis in tagged and untagged cells accumulated from all 6 reproducibility studies. Study #1 (navy), study #2 (purple), study #3 (Blue), study #4 (Olive), study #5 (Pink) & study # 6 (Orange). Third degree polynomial composite curve fit equation for tagged cells: $y = 1.945 + 0.187x - 0.002x^2 + 1.161E^{-5}x^3$ ($R^2 = 0.523$), for untagged cells: $y = 1.570 - 0.013x + 1.918E^{-4}x^2 - 8.8680E^{-7}x^3$ ($R^2 = 0.085$). The red line of best fit is the line of best fit generated from the average of the coefficients calculated in Table 3.

An inter-experimental relaxation normalization was performed for comparison between all 6 studies. This normalization was carried out using ratios calculated in Table 4. Study # 1 was used as an example to display how the values for T_2 were normalized using their corresponding normalization ratios. This example can be found in Table 5 and Figure 34. All normalized R_2 values were then plotted versus their original percentages of apoptotic damages and are found in Figure 35.

Table 4: Average T_2 values of untagged populations from each reproducibility study analyzed to generate ratios to be used for an inter-experimental normalization.

Reproducibility Study #	Avg T2(ms)(Untagged)	Normalization Ratio
1	905.84	905.84/746.88
2	752.28	752.28/746.88
3	623.59	623.59/746.88
4	678.95	678.95/746.88
5	693.93	693.93/746.88
6	826.69	826.69/746.88
Overall Avg T2(ms) (Untagged)	746.88	
Standard Deviation	104.20	

Table 5: An example of the method of normalization for reproducibility study #1. Note that the inverse of the normalization ratio is used since the average T_2 of the untagged population is greater than the overall average of T_2 (untagged).

% Apoptosis	T2 (ms)	Normalization Ratio	Normalization Formula	Normalized T2 values (ms)
11.02	366.7	746.88/905.84	366.7*(746.88/905.84)	302.35
24.55	231.04	746.88/905.84	231.04*(746.88/905.84)	190.5
39.53	162.88	746.88/905.84	162.88*(746.88/905.84)	134.3
53.95	156.5	746.88/905.84	156.5*(746.88/905.84)	129.04
70.57	138.45	746.88/905.84	138.45*(746.88/905.84)	114.15
98.08	135.8	746.88/905.84	135.8*(746.88/905.84)	111.97

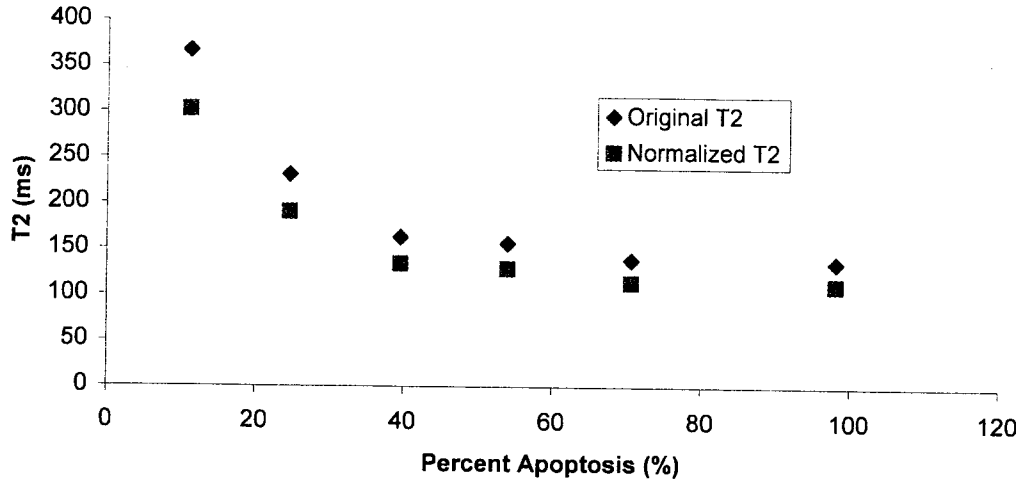

Figure 34: The relationship between the original T_2 and the normalized T_2 values and the percent of apoptosis in reproducibility study #1.

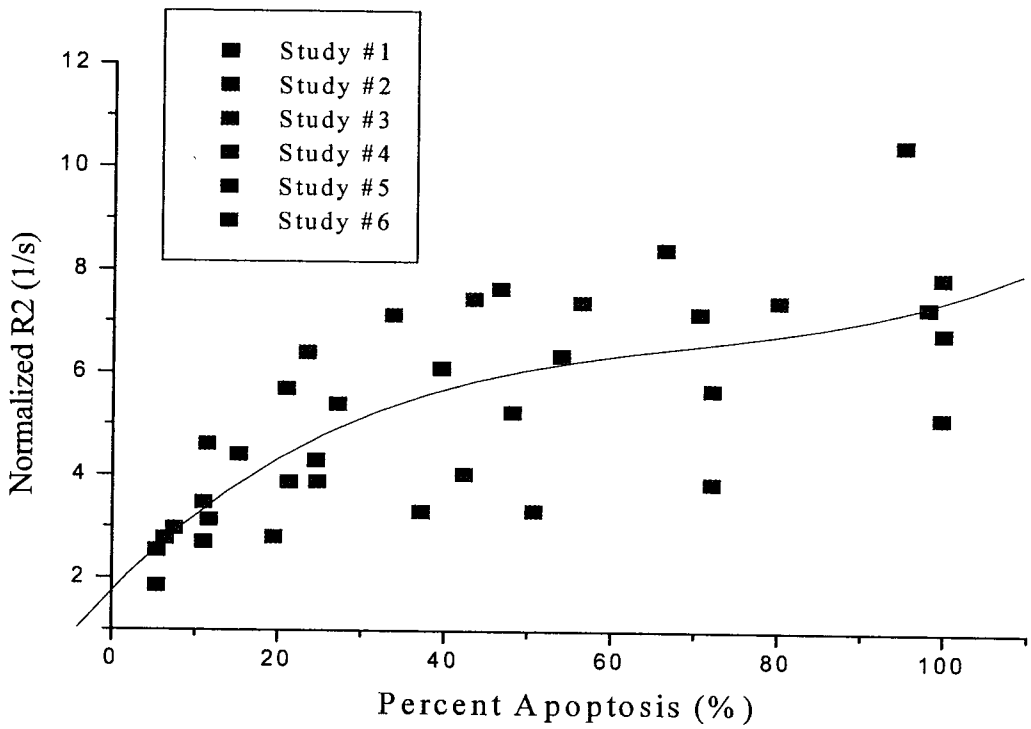

Figure 35: The relationship between the normalized R_2 values of all 6 reproducibility studies combined for comparison. The curve of best fit equals $y = 1.7543 + 1671x - 0.0021x^2 + 1.0232x10^{-5}x^3$, ($R^2 = 0.5508$).

The results of the inter-experimental spread addressed by the normalization of controls (untagged data) does not increase the overall quality of reproducibility of this technique. After all T_2 values were normalized the coefficient of regression only changed from 0.523 to 0.5508.

An investigation to confirm the unique correlation between the variables was performed to verify that the individual studies do in fact share a common polynomial curve fit. This was done using vertical shifts displayed in Table 6. The vertical shifts were calculated using the third order polynomial fit equations for each individual curve and placing a common point (at 50% apoptosis) between them all. This correlation cannot determine any quantifiable significance yet it visually determines that when the apoptotic percentage increases the relaxation rate does in fact follow this trend throughout each study. This vertical shift analysis can be found in figure 36 and the average relationship is determined to be $y = 2.792 + 0.155x - 0.002x^2 + 1.058E^{-5}x^3$ ($R^2 = 0.814$) for all reproducibility studies after the vertical shifts were made.

Table 6: Analysis of reproducibility studies #1-6 after vertical shifts were made.

Study #	Y-Axis Shift
1	0.619
2	-2.7734
3	-0.8243
4	1.4897
5	0.5818
6	2.1333

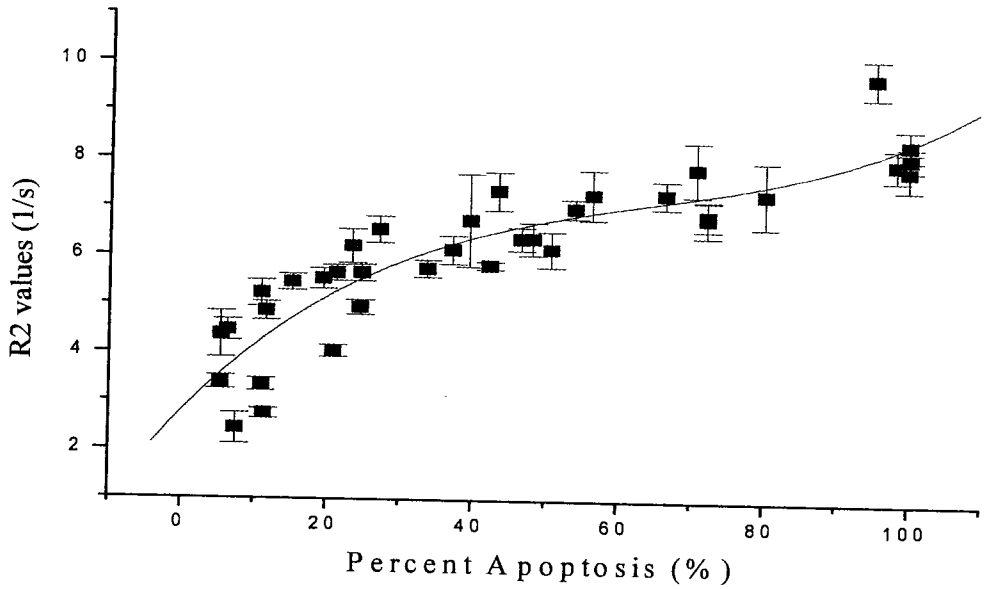

Figure 36: The comparison of all 6 reproducibility studies after vertical shifts were made. R_2 determined by MRI analysis. Third degree polynomial fit equation for tagged cells: $y = 2.792 + 0.155x - 0.002x^2 + 1.058E^{-5}x^3$ ($R^2 = 0.814$).

4.6.3. Discussion

Evaluating each reproducibility study carefully using curve fitting analysis we can determine that R_2 and percentage of apoptotic cells have a unique polynomial trend relationship. All of the studies can be characterized by a shape which most closely follows a 3rd order polynomial in R_2 as percentage of apoptotic cells increases rather than following a standard linear trend that literature would have predicted [41, 43]. We would expect a high correlation between the R_2 and percent apoptosis, and indeed in each of the 6 studies the correlation coefficients are found to be between 0.9344 and 0.9978. These functional coefficients provide a useful quantification of the strength of the relationship between R_2 and percent apoptosis. All the studies (excluding #4 since its maximum

percentage of apoptosis only reaches <50%) have R_2 values that range over approximately 4.79 s^{-1} during the gradient of approximately 5-100% apoptosis. One similarity between all the studies involves their minimum sensitivity at a low percentage of apoptosis. Even at the smallest percent of apoptosis (untreated cell population) the contrast is visible and the quantitative R_2 value is able to differentiate between the populations. This indicates that approximately 5% of 300 cells [(60 x 10^6 cells/mL)* (100uL)] is enough to differentiate between healthy cells that are untagged and tagged. Approximately 5% apoptosis occurs in healthy cells and this acts as a baseline for untreated cells. So therefore, our method does appear to be sensitive enough to detect the background (or naturally occurring apoptotic level), which we know to be approximately 5%. Since at any time in the human body there is usually <10% apoptosis occurring, this tool has the potential to differentiate between healthy and apoptotic cells even prior to oxidative stress inducing an increase in apoptosis.

If the annexin V SPIO nanoparticles are binding selectively to the externalized PS from apoptotic cells the decrease in T_2 must then be caused by the increase in iron oxide particles present in the sample. For this assumption to be made, the binding efficiency of annexin V to PS must be analyzed. This is done by introducing basic MicroBeads (SPIO only) to the percent apoptosis gradient. If the basic MicroBeads were to cause significant change in relaxation times to apoptotic cells then the results would have indicated that the increase in R_2 is not only caused by the increase of externalized PS, but also contribution from residual SPIO. It is important to show that the increase in R_2 is characteristic of the apoptotic cells and must reflect the amount of PS available to be bound. These basic MicroBeads should not be able to bind to cells and thus should not change the relaxation

times of the samples, otherwise the experimental hypothesis would be disproved. Fortunately, the annexin V-SPIO nanoparticles were the only particles capable of binding to the apoptotic cells when compared with the basic MicroBeads relative to the untagged population and thus the specificity of the annexin V to PS was shown (see Figure 26). The results show no significant increase in R_2 due to basic MicroBeads and thus SPIO are only bound to the apoptotic cells if annexin V is present. This would also demonstrate that the rinsing during the procedure is working, and there is no excess SPIO present in the samples. Therefore, the R_2 values are an accurate quantitative method in determining the amount of apoptotic cells present. The specificity of annexin V has also been demonstrated by Blankenberg using annexin V-99mTc in vivo. The ability to recognize target cells with high affinity and specificity is yet another characteristic that the SPIO nanoparticles should entail.

It should be noted that any real cell population will always contain some degree of apoptosis (see first data on each reproducibility study). Assume a hypothetical cell population in which no cells are apoptotic. Since we have shown that the excess SPIO nanoparticles are being rinsed thoroughly during the procedure we would expect there to be no external PS available for annexin V binding. In such an experiment, there would be no SPIO present in the MRI sample thus mimicking the controls. As mentioned, real healthy cell population always contain some degree of apoptosis (shown by the first point in each study graph). In order to check the consistency of the results, an extrapolation of the 3rd order polynomial curve fittings to zero percent apoptosis was performed and was compared to the average R_2 value of the untagged control population for each study (see

Table 7). Even when tagged with annexin V-SPIO, the R_2 values should converge with controls of untagged populations at zero apoptosis.

Table 7: A comparison of the average T_2 & R_2 values for the untagged populations to the extrapolated values at zero percent apoptosis for each reproducibility study. Delta R2 is the difference between the tagged zero percent apoptosis R2 value and the average untagged R2 value for each study.

Study #	Average T_2 value (untagged) (ms)	Average R_2 value (untagged) (1/s)	R_2 extrapolated to 0% apoptosis (tagged)(1/s)	Delta R_2 (1/s)
1	905.84	1.104	1.074	-0.030
2	752.28	1.329	2.849	1.520
3	623.59	1.604	0.866	-0.738
4	678.95	1.473	1.882	0.409
5	693.93	1.441	1.734	0.293
6	826.69	1.210	1.701	0.491
			Average Delta R_2	0.324
			Standard Deviation	0.737

As seen in Table 7, the average and standard deviation of ΔR_2 values for all 6 studies was calculated to be 0.324 +/- 0.737 s^{-1}. This standard deviation is consistent with the statistics determined for the average y-intercept (coefficient A) of all the reproducibility studies found in Table 3 which was determined to be 1.6843 +/- 0.698 s^{-1}. Also note that the standard deviation of 0.737 s^{-1} is small relative to the scatter of any given point of the reproducibility study which is seen to be as much as 5 s^{-1} (see Figure 33). Overall, this suggests excellent intra-experimental self consistency for each reproducibility study (ie. the percent apoptosis curves relative to the controls).

However, our studies show rather poor inter–experimental reproducibility which can be seen by the large spread of T_2 values between each study. The inter-experimental normalization average T_2 of the untagged populations was calculated to be 746.88 ms with a standard deviation of 104.2 ms (see Table 4). This is a large standard deviation to

have since untagged cells should have no change in the relaxation time at all. This discrepancy between T_2 values for untagged cells does in fact point out that something in this method is very inconsistent. Controls of untagged cells should be much more reproducible, however, when it comes to human cells there are many biological factors (ie. cell cycle, cell count approximations, variations in wells etc.) that have been known to generate inconsistencies. Even cell clonogenic assays produce scatter due to variations in cells[48].

Even though the y-intercepts (coefficient A) for all of the studies were more reproducible than any other percentage of apoptotic damage, the range varied from 0.866 s^{-1} to 2.849 s^{-1} (refer to Table 3) thus suggesting that this method may not give an exact quantitative measure of any given apoptotic cell percentage (approximately 41.5% error) but might provide the ability to estimate the approximate degree of apoptotic damage. For instance, when classifying different damage levels (ie. 0-25%, 0-50% etc.) and comparing them to that of the zero percent apoptotic level it narrows down the range of cell damage that has been induced in the sample. This can be seen in Table 8 as an increase in ΔR_2 between damage levels defined.

Table 8: A comparison of delta R2 values for specific damage levels (ranges of apoptosis)

	Delta R2 values at 25, 50, 75 & 100% Apoptosis			
Study	25%	50%	75%	100%
1	3.30	5.18	6.06	6.36
2	4.63	6.41	7.49	10.00
3	6.27	8.04	8.28	10.00
5	3.73	3.75	2.63	2.90
6	1.90	2.53	3.08	4.80
Average	3.97	5.18	5.51	6.81
St. Dev	1.62	2.17	2.55	3.16

The average and standard deviations for the change in R_2 found in Table 8 indicate that there is significant overlap between the intervals chosen. Clearly the only damage level with a statistically significant delta R_2 is between 0-25% apoptosis. This indicates that this technique may only be useful for detecting such lower levels of apoptotic damage. For a more accurate depiction of the levels of apoptotic damage we turn to the notion that the sensitivity of our assay can be characterized by the slope of the R_2 vs % apoptosis curve. Figure 37 shows the slope of R_2 vs % apoptosis for each reproducibility study. By analyzing these curves and determining an average for all 6 reproducibility studies (displayed in Figure 38) we can see the greatest slope of ΔR_2 occurs between 0% and approximately ~45% apoptosis. Between the percentages of 45% to approximately ~75% the change in R_2 (ΔR_2) values is minimal and thus making these values difficult to differentiate based on R_2. After approximately 75% apoptosis the slope increases making the change in R_2 large enough to differentiate between these ranges of apoptosis. In summary, the greatest change in R_2 values occurs prior to ~45% apoptosis and after ~75% and during the interval between them, the percentages of apoptosis are difficult to differentiate based on R_2 quantification.

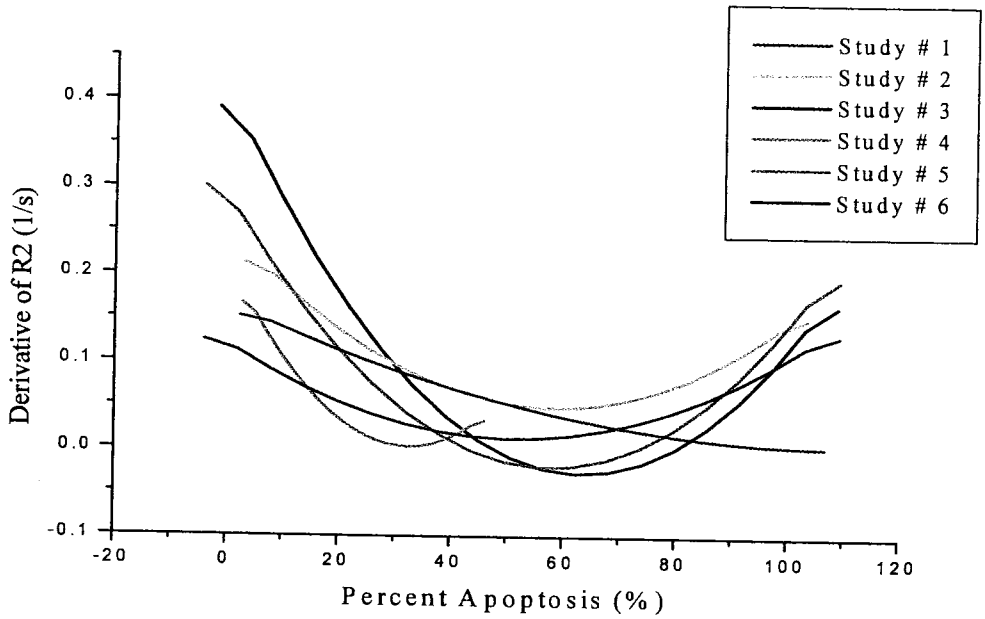

Figure 37: Derivative analysis of all 6 reproducibility studies indicating in which intervals of apoptosis display the greatest change of R_2 as a function of apoptotic damage.

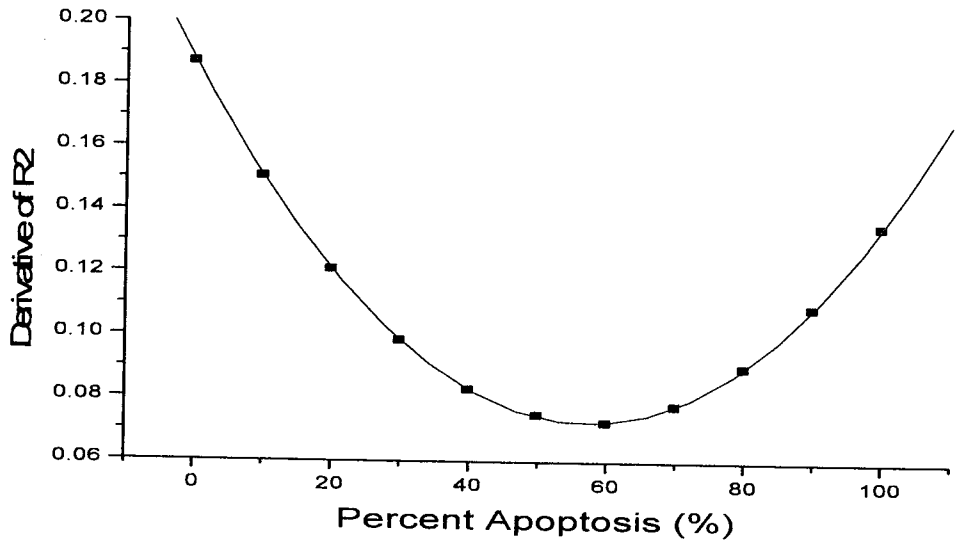

Figure 38: The average derivative of all 6 reproducibility studies indicating which intervals of apoptosis display the greatest change in R2 as a function of apoptotic damage. Equation of best fit: $y = 0.187 - 0.004x + 3.48E^{-5}x^2$.

4.6.3.1. Comparison of Results to Literature

Annexin V functionalized cross-linked iron oxide (CLIO) nanoparticles were first presented by Schellenberger et al.[38] who demonstrated the ability of this iron oxide nanoparticle to specifically decrease the signal intensity of the camptothecin-treated Jurkat T-cells in T_2 weighted images[45]. As an alternative to annexin V, iron oxide particles have also been labeled with the PS-binding C2A domain of the protein synaptotagmin I, which was successfully allowed the detection of apoptotic cells both in vitro[46] and in vivo[45]. Our results for the apoptosis gradient were different than reported values which could be due to the specific cell line used, the change in iron composition and the presence of other nonspecific cells[43]. It is difficult to compare R_2 values to those found in literature since they have used different cell types, different cell concentrations different pulse sequences and parameters and a polynomial trend relationship has never been found. It was Rad who first reported that relaxation parameters depend on cell type and size since equal amounts of iron particles in different cells results in different MR output values[43]. Sosnovik was able to differentiate between degrees of apoptosis in cardiomyocytes using a gradient echo sequence and determined ΔR_2^* over a range of 30% to be 0.4 s^{-1}/ (% apoptosis)[41]. This is much more sensitive than the initial attempt at linear fitting (seen in Figure 26) which determined ΔR_2 over a range of 100% (at 120 x 10^6 cells/mL) to be only 0.1607 s^{-1}/ (% apoptosis). This indicates that measuring R_2^* would be a better quantification method for degrees of apoptosis, but this will be addressed in future work.

5. Conclusions

In this study Macs Annexin V MicroBeads were found to have a positive linear correlation between its concentration in a sample and the relaxation rate (R_2) measured with an MRI. The more SPIO nanoparticles in a sample, the faster the spin magnetization vectors will dephase, leading to a shorter transverse relaxation time (T_2). The ability to decrease relaxation time T_2 and the ability to bind to apoptotic cells (exposure of PS) together provide a method of apoptosis detection *in vitro*.

In this investigation, a method for detecting apoptosis *in vitro* was developed using annexin V for targeting of SPIO nanoparticles to PS. Our results indicate that apoptotic cells tagged by PS targeted SPIO nanoparticles have a shorter T_2 value than healthy cells and appear less intense in a T_2 MRI image. The sensitivity (ΔR_2/ %apoptosis) of this contrast can be enhanced by increasing the concentration of cells in the sample since they were found to be directly proportional. The apoptosis gradient studies determined a reproducible relationship between the degree of apoptotic damage and the relaxation rate R_2. Interestingly enough, the correlation between R_2 and percent of cells that were apoptotic wasn't as direct as literature would have expected[43,41]. Previously, researchers have determined a linear correlation between R_2 and percent apoptosis using a different type of SPIO nanoparticles, a different cell line and different pulse sequences to measure T_2. Through a series of experiments, the mean relationship between R_2 and percent apoptosis was determined to be $y = 1.945 + 0.187x - 0.002x^2 + 1.161E^{-5}x^3$ ($R^2 = 0.523$) for tagged cells and $y = 1.570 - 0.013x + 1.918E^{-4}x^2 - 8.8680E^{-7}x^3$ ($R^2 = 0.085$) for untagged cells. This implies that the variation in R_2 can predict variations in percent apoptosis but the relationship is not completely understood at this time. Even after the

inter-experimental relaxation normalization, it was still clear that this technique was very poorly reproduced. The shapes of the curves are similar indicating that the relationship is a 3rd order polynomial, yet the values of R_2 are not yet precise enough to use as a forecasting tool to predict the amount of apoptosis (only 52.3% of R_2 values are explained by a percentage of apoptosis shown in the R^2 value). There could be many reasons for the cause of this oddly shaped relationship between R_2 and percent apoptosis. The reasons affecting the unexpected shape of the curve have not been considered at this point in the investigation.

This detection method of PS in early stage apoptosis using SPIO nanoparticles can potentially be used to monitor the effectiveness of a given cancer therapy. Using the 3rd order polynomial trend that was established for Macs MicroBeads, one can differentiate between levels of apoptotic damage. Following cancer treatment, a patient could be injected with SPIO nanoparticles and then the level of tumour cell death could be quantified using this mMRI technique. However, at this stage the quantified R_2 values are not reproducible between experiments and may vary depending on the patient.

6. Future Work

In order to conclude the characterization of the MACS MicroBeads bound to cells, variation in temperature and MRI sequence technique effects on measured relaxivity enhancement should be investigated. Also, literature has shown that the gradient echo sequence has enhanced sensitivity showing a greater sensitivity with ΔR_2^* than ΔR_2 with single spin echo imaging sequence therefore could be a better technique to use for this investigation in the future [18]. In addition, literature also suggests that the balanced steady state free precession sequence could be optimized and show great results with human patients in the future since it is a very quick sequence[47] as well. The balanced steady state free precession (b-SSRP) sequence (also known as FIESTA or TRUE-FISP) imaging method has been shown to provide similar sensitivity as gradient echo imaging and a spin echo-like sensitivity to background magnetic field inhomogeneities[39]. Therefore analysis of ΔR_2^* would be the next step to increase sensitivity in this investigation.

Since our methods did not lead to precise results for detecting apoptosis *in vitro* then a new cell line or new morphological change of apoptosis should also be investigated. The HL-60 cell line has known to be a very resistant cell line to radiation[48]. If the transition were to occur from heat shock to radiation for induction of apoptosis, a more radiation sensitive cell line would be desired. Another morphological change in the apoptotic pathway to be analyzed could be nuclear fragmentation since it has shown promise in the detection of apoptosis. Since oligonucleosomes are released into the bloodstream during apoptosis, one could take a blood sample and analyze it, which could be proven more clinically useful.

7. References

[1] Fahlvik, A.K., J. Klaveness, and D.O. Stark, *Iron Oxides as MR Imaging Contrast Agents.* Journal of Molecular Resonance Imaging, 1993. **3**: p. 187-194.

[2] Alberts, B., et al., *Molecular Biology of the Cell.* fourth ed. 2002, New York, NY: Garland Science.

[3] MacKinnel, R.G., *et. al, The Biological Basis of Cancer.* 1999, Cambridge, UK: Cambridge University Press.

[4] Kerr, J.F.R., C. Winterford, M., and B. Harmon, V., *Apoptosis.* Cancer, 1994. **73**(8): p. 2013-2026.

[5] Strauss, H.W., et al., *Translational Imaging: Imaging of Apoptosis.* Handbook of Experimental Pharmacology, 2008: p. 259-75.

[6] Kerr, J.F.R., A.H. Wyllie, and A.R. Currie, Apoptosis: a basic biological phenomenon with wide-ranging implications in tissue kinetics B Journal of Cancer, 1972. **26**: p. 239-57.

[7] Potten, C. and J. Wilson, *Apoptosis: The life and death of cells.* 2004: Cambridge University Press.

[8] Hakumaki, J.M. and T. Liimatainen, *Molecular imaging of apoptosis in cancer.* European Journal of Radiology, 2005. **56**: p. 143-153.

[9] Brauer, M., *In vivo monitoring of apoptosis.* Neuro-Psychopharmacology & Biological Psyciatry, 2003. **27**: p. 323-331.

[10] Gewies, A., *Introduction to Apoptosis*, in *ApoReview*. 2003. p. 1-26.

[11] Tait, J.F., C. Smith, and F.G. Blankenberg, *Structural Requirements for In Vivo Detection of Cell Death with 99mTc-Annexin V.* The Journal of Nuclear Medicine, 2005. **46**(5).

[12] Boersma, H.H., et al., *Past, Present, and Future of Annexin A5: From Protein Discovery to Clinical Application.* The Journal of Nuclear Medicine, 2005. **46**(12): p. 2035-2050.

[13] Koopman, G., et al., *Annexin V for Flow Cytometric Detection of Phosphatidylserine Expression on B Cells Undergoing Apoptosis.* Blood, 1994. **84**(5): p. 1415-1420.

[14] Company, B.D.a., *BD Biosciences Canada.* 2007.

[15] Gerke, Moss SE. *Annexins: from structure to function.* Physiol. Rev. 2002; **82** (2): p. 331-371

[16]Blankenberg, F.G., et al., *In vivo detection and imaging of phosphatidylserine expression during programmed cell death.* Proc. Natl. Acad. Sci., 1998. **95**: p. 6349-6354.

[17] Artenov, D., *Magnetic Resonance Imaging With Targeted Contrast Agents.* Journal of Cellular Biochemistry, 2003. **90**: p. 518-524.

[18] Majumbdar, S., S.S. Zoghbi, and J.C. Gore, *The Influence of Pulse Sequence on the Relaxation Effects of Superparamagnetic Iron Oxide Contrast Agents.* Magnetic Resonance in Medicine, 1989. **10**: p. 289-301.

[19] Slichter, C.P., *Principles of Magnetic Resonance*, ed. F. Seitz. 1963: Harper & Row Publishers.

[20] Morris, P.G., *Nuclear Magnetic Resonance Imaging in Medicine and Biology*. 1986: Oxford University Press.
[21] Chen, C.N. and D.I. Hoult, *Biomedical Magnetic Resonance Technology*. Medical Science Series. 1989: Adam Hilger IOP Publishing ltd.
[22] McMillan, J.A., *Electron Paramagnetism*, ed. R.B. Corporation. 1968: Chapman-Reinhold Inc.
[23] Haacke, E.M., et al., *Magnetic Resonance Imaging: Physical Principles and Sequence Design*. 1999: John Wiley & Sons Inc. Publication.
[24] Callaghan, P.T., *Principles of Nuclear Magnetic Resonance Microscopy*. 1991: Oxford Science Publications.
[25] Weissleder, R., *Molecular Imaging in Cancer*. Science Magazine, 2006. **312**: p. 1168-1171.
[26] Harisinghani, M.G., et al., *Noninvasive Detection of Clinically Occult Lymph-Node Metastases in Prostate Cancer*. The New England Journal of Medicine, 2003. **348**(25): p. 2491-2499.
[27] Thorek, D.L.J., et al., *Superparamagnetic Iron Oxide Nanoparticle Probes for Molecular Imaging*. Annals of Biomedical Engineering, 2006. **34**(1): p. 23-38.
[28] Baert, A.L. and M. Knauth, *Contrast Media: Safety Issues and ESUR Guidelines*. 2nd ed. Medical Radiology, Diagnostic Imaging, ed. T.H. S. and W.J.A. W. 2009. 205-212.
[29] Qaio, R., C. Yang, and M. Gao, *Superparamagnetic iron oxide nanoparticles: from preparations to in vivo MRI applications*. Journal of Materials Chemistry, 2009. **19**: p. 6274-6293.
[30] Wang, Y.-X.J., S.M. Hussain, and G.P. Krestin, *Superparamagnetic iron oxide contrast agents: physiochemical characteristics and applications in MR imaging*. European Journal of Radiology, 2001. **11**: p. 2319-2331.
[31] Bautista, M.C., et al., *Comparative study of ferrofluids based on dextran coated iron oxide and metal nanoparticles for contrast agents in magnetic resonance imaging*. Nanotechnology, 2004. **15**: p. 5154-5159.
[32] Josephson, L., *The Effects of Iron Oxides on Proton Relaxivity*. Magnetic Resonance Imaging, 1988. **6**: p. 647-653.
[33] Nishie, A., et al., *In vitro imaging of human monocytic cellular activity using superparamagnetic iron oxide*. Computerized Medical Imaging and Graphics, 2007. **31**: p. 638-642.
[34] Metz, S., et al., *Capacity of human monocytes to phagocytose approved iron oxide MR contrast agents in vitro*. European Radiology, 2004. **14**: p. 1851-1858.
[35] Ning, S. and S.J. Knox, *G2/M-phase arrest and death by apoptosis of HL60 cells irradiated with exponentially decreasing low-dose-rate gamma radiation*. Radiat. Res., 1999. **151**(6): p. 659-669.
[36] Watson, N.C. et. al., *Radiosensitization of HL-60 human leukemia cells by bryostatin-1 in the absence of increased DNA fragmentation or apoptotic cell death*. International Journal of Radiation Biology, 1996. **69**(2): p. 183-192.
[37] Torigian, D.A., *Functional Imaging of Cancer with Emphasis on Molecular Techniques*. CA: A Cancer Journal for Clinicians, 2008. **57**: p. 206-224.

[38] Schellenberger, E.A., et al., *Magneto/Optical Annexin V, a Multimodal Protein.* Bioconjugate Chem., 2004. **15**: p. 1062-1067.
[39] Liu, C.H., et al., *MR contrast probes that trace gene transcripts for cerebral ischemia in live animals.* The FASEB Journal, 2007. **21**: p. 3004-3015.
[40] Zhou, J., et al., *A rapid method for detecting conformational changes during differentiation and apoptosis of HL-60 cells by Fourier-transform infrared spectroscopy.* Biotechnol. Appl. Biochem., 2001. **33**: p. 127-132.
[41] Sosnovik, D.E., et al., *Magnetic Resonance Imaging of Cardiomyocyte Apoptosis with a Novel Magneto-Optical Nanoparticle.* Magnetic Resonance in Medicine, 2005. **54**: p. 718-724.
[42] Kato, H. et al. *Composition of MRI phantom equivalent to human tissues.* Medical Physics, 2005. **32** (10)
[43] Rad, A.M., et al., *Quantification of Superparamagnetic Iron Oxide (SPIO)-Labeled Cells Using MRI.* Journal of Magnetic Resonance Imaging, 2007. **26**: p. 366-374.
[44] Kuhlpeter, R., et al., R2 and R2* Mapping for Sensing Cell-bound Superparamagnetic Nanoparticles: In Vitro and Murine in Vivo Testing. Radiology, 2007. **245**(2): p. 449-457.
[45] van Tilborg, G.A.F., et al., *Internalization of annexin A5 functionalized iron oxide particles by apoptotic jurkat cells.* Contrast Media and Molecular Imaging, 2009. **4**: p. 24-32.
[46] Jung, H.-i., et al., *Detection of Apoptosis Using the c2A Domain of Synaptotagmin I.* Bioconjugate Chem., 2004. **15**(983-987).

[48] Lehnert, S., et al., *Radiation Response of Haematopoietic Cell Lines of Human Origin.* International Journal of Radiation Biology, 1985. **49**(3): p. 423-431.